Accurate space-based NOx emission estimates with the flux divergence approach require fine-scale model information on local oxidation chemistry and profile shapes

Felipe Cifuentes[1,2], Henk Eskes[1], Enrico Dammers[3,4], Charlotte Bryan[1], and Folkert Boersma[2,1]

[1]R&D Satellite Observation department, Royal Netherlands Meteorological Institute (KNMI), De Bilt, 3731 GA, The Netherlands

[2]Meteorology and Air Quality department, Wageningen University & Research (WUR), Wageningen, 6708 PB, The Netherlands

[3]Air Quality and Emissions Research, Netherlands Organisation for Applied Scientific Research (TNO), Utrecht, 3584 CB, The Netherlands

[4]Institute of Environmental Sciences (CML), Leiden University, Leiden, 2333 CC, The Netherlands

Correspondence: Felipe Cifuentes (felipe.cifuentescastano@knmi.nl)

Abstract. The flux divergence approach (FDA) is a popular technique for deriving NO_x emission estimates from tropospheric NO_2 columns measured by the TROPOMI satellite sensor. An attractive aspect of the FDA is that the method simplifies three-dimensional atmospheric chemistry and transport processes into a two-dimensional (longitude-latitude) steady-state continuity equation for columns that balances local NO_x emissions with the net outflow and chemical loss of NO_x. Here we test the capability of the FDA to reproduce known NO_x emissions from synthetic NO_2 column retrievals generated with the LOTOS-EUROS chemistry transport model over the Netherlands at high spatial resolution of about 2x2 km during summer. Our results show that the FDA captures the magnitude and spatial distribution of the NO_x emissions to high accuracy (absolute bias <9%), provided that the observations represent the NO_2 column in the boundary layer, that wind speed and direction are representative for the boundary layer (PBL) column, and that the high resolution spatiotemporal variability of the NO_2 lifetimes and NO_x:NO_2 ratio is accounted for in the inversion, instead of using single fixed values. The FDA systematically overestimates NO_x emissions by 15-60% when using tropospheric NO_2 columns as the driving observation, while using PBL NO_2 columns largely overcomes this systematic error. This merely reflects that the local balance between emissions and sinks of NO_x occurs in the boundary layer, which is decoupled from the NO_2 in the free troposphere. Based on the recommendations from this sensitivity test, we then applied the FDA using observations of NO_2 columns from TROPOMI, corrected for contribution from free tropospheric NO_2, between 1 June and 31 August 2018. The NO_x emissions derived from the default TROPOMI retrievals are biased low over cities and industrialized areas. However, when the coarse 1x1 degree TM5-MP NO_2 profile used in the retrieval is replaced by the high-resolution profile of LOTOS-EUROS, the TROPOMI NO_x emissions are enhanced by 22% and are in better agreement with the inventory for the Netherlands. This emphasizes the importance of using realistic high-resolution *a-priori* NO_2 profile shapes in the TROPOMI retrieval. We conclude that accurate quantitative NO_x emissions estimates are possible with the FDA, but that they require sophisticated, fine-scale, corrections for both the NO_2 observations driving the method, as well as the estimates of the NO_2 chemical lifetime and NO_x:NO_2 ratio.

This information can be obtained from high-resolution chemistry transport model simulations, at the expense of the simplicity and applicability of the FDA.

1 Introduction

Nitrogen oxides ($NO_x = NO + NO_2$) are highly reactive atmospheric trace gases, primarily originating from fossil-fuel combustion in mobile and industrial sources, as well as biomass burning, microbial activity in soils, and lighting (Song et al., 2021; Murray, 2016). These compounds contribute to the formation of tropospheric ozone and secondary aerosols (Seinfeld and Pandis, 2006); thereby causing negative implications for human health, climate, and terrestrial and aquatic ecosystems (Clark et al., 2013; de Vries, 2021). Accurate and regularly updated emission inventories combined with observations are needed to assess the current pollution levels, formulate control measures, and track their effectiveness.

Conventional bottom-up approaches to estimate NO_x emissions rely on combining aggregated activity data, average emission factors, and spatiotemporal proxies for disaggregation. These methods have considerable uncertainties due to factors such as omitted sources, an incomplete comprehension of sectoral activity, real-world operating conditions, and spatial distribution of sources (Pommier, 2022; Lonsdale and Sun, 2023; Liu et al., 2022). Moreover, the estimates are outdated by at least a year, due to the time required to collect the data (Wang et al., 2020; Zhang et al., 2023).

In contrast, satellite observations, available in real-time, provide comprehensive and independent information about the global distribution of the total amount of NO_2 in the atmosphere with city-scale resolution, allowing the quantification of major point sources (Beirle et al., 2021, 2023; Chen et al., 2023; Dammers et al., 2022; Fioletov et al., 2022). These observations can be linked to emissions by accounting for the chemical conversion and transport of the atmospheric NO_2 (Liu et al., 2022). The satellite-based emissions hence provide up-to-date information obtained by observing real operating conditions, can track the time dependence of emissions, and facilitate the identification of overlooked sources due to their full spatial coverage (Pommier, 2022; Lorente et al., 2019).

Despite providing valuable insights, satellite-derived emissions have limitations. NO_2 observations are limited to clear-sky conditions and only represent the atmospheric conditions close to the satellite overpass time. For polar sun-synchronous orbit satellites, the overpass occurs at a fixed local time, which excludes the estimation of diurnal emission profiles and may overlook significant sources inactive during the observations. Additionally, current satellites maintain a relatively coarse spatial resolution compared to specific regional bottom-up emission inventories that achieve kilometer or sub-kilometer scale. Satellite-derived emissions therefore supplement traditional bottom-up emission inventories rather than replace them, offering additional and complementary information, and a benchmark for validation because they are fully independent.

The TROPOspheric Monitoring Instrument (TROPOMI) (Veefkind et al., 2012) has been widely employed for deriving satellite-based NO_x emissions. The revolutionary pixel size at nadir of 3,5 km x 7 km (improved to 3,5 km x 5,5 km after

August 2019), and the high signal-to-noise ratio, make the product suitable for examining emissions from diverse sources such as city emissions (Lorente et al., 2019; Pommier, 2022; Xue et al., 2022; Zhang et al., 2023), power plants (Goldberg et al., 2019; Saw et al., 2021; Skoulidou et al., 2021a; Krol et al., 2024), oil and gas production (Dix et al., 2022), individual ships (Georgoulias et al., 2020; Kurchaba et al., 2022; Riess et al., 2024), lighting (Allen et al., 2021; Zhang et al., 2022), soil (Lin et al., 2023) and croplands (Huber et al., 2020). Beyond the NO_x emissions, the TROPOMI instrument has also been employed to derive emission datasets for CH_4 (Liu et al., 2021), SO_2 (Chen et al., 2024; Fioletov et al., 2020) and CO (Leguijt et al., 2023).

Diverse methods have been employed to estimate satellite-based emissions. Chemical transport models (CTM) based approaches use satellite data as a constraint to enhance the emission inventory, using techniques such as mass balance (Cooper et al., 2017), variational data assimilation (Yarce Botero et al., 2021), Kalman filters (Ding et al., 2017), and analytical inversion (Lu et al., 2022). While CTM-based methods incorporate detailed three-dimensional chemical and meteorological processes allowing to obtain spatiotemporally resolved emissions, their application is constrained by the requirement for additional input datasets and computational expenses (Lonsdale and Sun, 2023). On the other hand, CTM-independent approaches are based on plume dispersion models or local mass conservation applying a steady-state continuity equation. Plume dispersion methods involve fitting a dispersion model to the concentration data across the affected area to derive emissions, requiring a precise definition of the region influenced by plume advection. In contrast, local mass conservation methods operate at the source or pixel level, which eliminates the need to define a specific region of interest and allows for the simultaneous estimation of multiple sources (Misra et al., 2021).

Beirle et al. (2019) proposed a flux divergence approach (FDA) based on the steady-state continuity equation for NO_2 columns to extract surface NO_x emissions. This method uses satellite observations of NO_2 vertical column densities (VCD) and requires knowledge of horizontal wind components, a conversion factor from NO_2 to NO_x, and the chemical lifetime of NO_2 at satellite overpass time. Different authors applied this methodology to estimate NO_x emissions at the global scale (Beirle et al., 2023) or for specific regions, such as the United States (Dix et al., 2022), North India (Misra et al., 2021), Egypt (Rey-Pommier et al., 2022), South Asia (de Foy et al., 2022), and Taiwan (Chen et al., 2023). In addition, few studies have evaluated the accuracy and limitations of FDA satellite-derived emissions by using synthetic observations generated through chemical transport models as input within their approach (Dix et al., 2022; Hakkarainen et al., 2022; Goldberg et al., 2022). In contrast, most other studies have primarily focused on evaluating the FDA's sensitivity to different parameters and on estimating uncertainties arising from input data. The major sources of uncertainty in the method are considered to be biases in the observed NO_2 VCD, due to reduced vertical sensitivity to near-surface NO_2 by the satellite products, and the influence of selected *a-priori* NO_2 vertical profile shapes (Douros et al., 2023). Additional sources of uncertainty include systematic biases in the zonal and meridional wind components and the altitude at which they are sampled, and faulty representation of the spatial and seasonal changes in NO_x lifetime and the NO_2 to NO_x conversion factors (Beirle et al., 2019, 2021, 2023).

This study aims to evaluate the accuracy with which known NO_x emissions can be reproduced by the FDA, identify its weaknesses and uncertain parameters, and provide recommendations for its application and improvement. Synthetic NO_2 VCD satellite observations at high spatial resolution, generated with the LOTOS-EUROS model (Schaap et al., 2008; Manders

et al., 2017), were used to derive a NO_x emission dataset using the FDA. The new dataset was compared qualitatively and quantitatively to the emissions originally ingested into the model to characterize the performance and quantify the various contributions to the uncertainty of the method. This study also delves into the impact of using high spatial resolution (2x2 km^2) chemical and meteorological fields to represent the variability of the NO_2 VCD profile shapes, NO_2 lifetime, and the NO_2 to NO_x conversion factors, and studies their importance in reconstructing accurate NO_x emission datasets. Furthermore, we will evaluate the applicability of the FDA for satellite observations at different times of day, different from the noon conditions of the TROPOMI overpass time, to assess the method's applicability throughout the day. This provided insights into the suitability of this method for geostationary observations.

2 Data

2.1 TROPOMI NO_2 tropospheric column

The TROPOMI instrument, on board of the Sentinel-5 Precursor (S-5 P) polar satellite, is a nadir-viewing spectrometer. It measures radiation across the ultraviolet, visible, and infrared spectral regions and is utilized for monitoring atmospheric trace gases and aerosols (Veefkind et al., 2012). NO_2 columns are retrieved following a three-step procedure. First, the NO_2 slant column density is derived from the L1b spectra measured by TROPOMI using a Differential Optical Absorption Spectroscopy (DOAS) fit. The slant column is divided into a stratospheric and tropospheric fraction using data assimilation within the TM5-MP model at a 1x1°horizontal resolution (Williams et al., 2017). Lastly, the slant columns are converted into VCD using total and altitude-dependent air mass factors (AMFs). The AMFs are dependent on the NO_2 vertical profiles derived from TM5-MP, the viewing geometry of the satellite, the surface albedo, surface pressure, and clouds and aerosols characteristics. Further description of the retrieval can be consulted at van Geffen et al. (2022a) and van Geffen et al. (2022b).

Routine validation of TROPOMI NO_2 observations against ground-based MAX-DOAS measurements at 29 stations revealed a mean bias of -28%, escalating to -40% over heavily polluted regions (Lambert et al., 2023). This bias is predominantly linked to the vertical profile generated by TM5-MP, which insufficiently resolves concentration hotspots and exhibits deviations in profile shape, particularly near the Earth's surface (Chan et al., 2020; Verhoelst et al., 2021). The discrepancies in TROPOMI observations can then be partially mitigated by updating the *a-priori* vertical profile with one derived from a higher-resolution air quality model (Griffin et al., 2019; Zhao et al., 2020; Judd et al., 2020; Douros et al., 2023). This procedure is done via TROPOMI averaging kernels and it is explained in the TROPOMI NO_2 Product User Manual (Eskes et al., 2022). Remaining biases in TROPOMI observations might arise from errors in the slant column, the stratospheric-tropospheric partitioning, and various factors affecting the air mass factor (AMF) beyond the *a-priori* profile, including surface albedo and cloud cover.

This study used the TROPOMI L2 NO_2 version 2.4.0 reprocessed product, focusing on orbits over the Netherlands from 1 June to 31 August 2018. During this period, TROPOMI's nadir pixel size was 3,5 km x 7 km. The equator overpass occurs around 13:30 local time. To enhance the data reliability, pixels with a quality assurance value below 0,75 were excluded, effectively removing pixels with cloud radiance fractions higher than 0,5 and minimizing the impact of uncertain retrievals (van Geffen et al., 2022a). Additionally, a local TROPOMI product was generated by replacing the TM5-MP *a-priori* with the

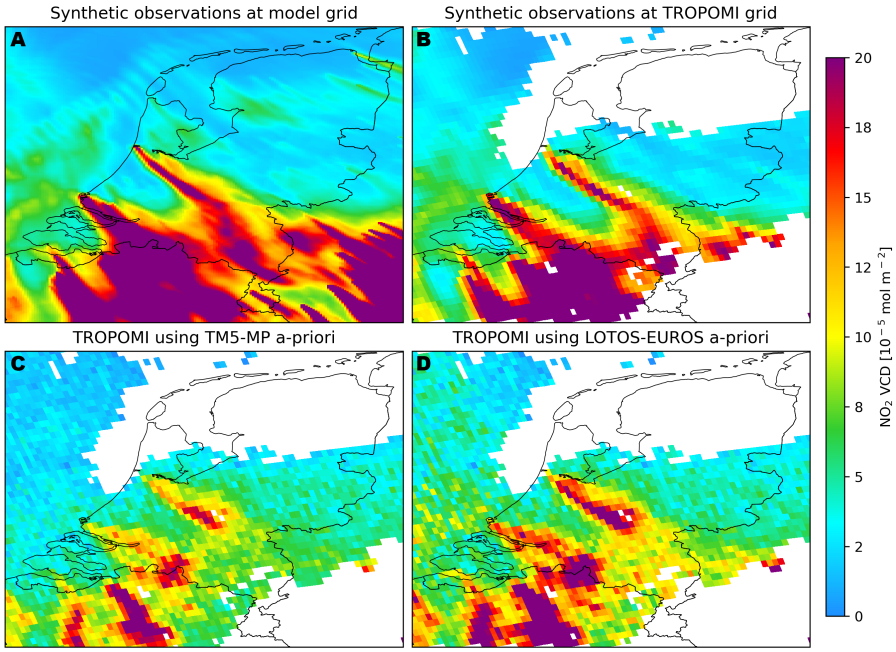

Figure 1. Comparison of NO_2 vertical column densities over the Netherlands on 5 July 2018, derived from synthetic and actual TROPOMI observations. **(A)** Synthetic observations at native LOTOS-EUROS resolution (2x2 km^2). **(B)** Synthetic observations spatiotemporally interpolated into the TROPOMI grid, and excluding the pixels where TROPOMI observations do not satisfy a quality assurance value over 0,75. **(C)** TROPOMI observations using the default TM5-MP *a-priori* profile shape. **(D)** TROPOMI observations using a high-resolution *a-priori* profile shape derived from the LOTOS-EUROS simulation.

one derived from the LOTOS-EUROS high-resolution simulations over the Netherlands (See section 2.2). Figure 1 show the variation in NO_2 VCD between the TM5-MP and LOTOS-EUROS TROPOMI products, showing a 23% increase in TROPOMI observed NO_2 VCD over heavily polluted areas when using LOTOS-EUROS *a-priori* NO_2 profiles. In contrast, background regions do not show significant enhancements.

2.2 Synthetic NO_2 observations

LOTOS-EUROS is an offline 3D CTM developed in the Netherlands. The model is used for operational forecast in the Netherlands and Europe (Manders et al., 2017). Its utility extends to research applications in diverse global regions, such as northwest South America (Yarce Botero et al., 2021) and China (Timmermans et al., 2017; Petersen et al., 2019). LOTOS-EUROS is part of the Copernicus Atmospheric Monitoring Service (CAMS) European air quality ensemble, a service that provides forecasts and reanalyses of the main air pollutants using 11 state-of-the-art CTMs. Within CAMS, LOTOS-EUROS undergoes routine validation with in-situ observations and TROPOMI satellite data, and is evaluated against the other ensemble members (Peuch et al., 2022). Additionally, independent studies have demonstrated good agreement between the simulated tropospheric NO_2

columns and those measured by TROPOMI and ground-based remote sensing instruments in the Netherlands (Vlemmix et al., 2015) and over Greece (Skoulidou et al., 2021b). These studies found discrepancies ranging from 1% to 35% when comparing LOTOS-EUROS columns with measurements from MAX-DOAS instruments. LOTOS-EUROS has also participated in numerous model intercomparison studies showing overall strong performance (Bessagnet et al., 2016; Colette et al., 2017; Vivanco et al., 2018).

In this study, the LOTOS-EUROS v2.2.009 model was used to generate an hourly high-resolution (2x2 km^2) NO_2 dataset across the Netherlands spanning from 1 June to 31 August 2018. The simulations were conducted using 12 vertical levels, extending from the ground to approximately 9 km above the earth's surface. Tropopause heights can exceed 15 km in tropical regions and typically between 8 and 12 km in other areas (Xian and Homeyer, 2019). Given that this study focuses on the Netherlands, using vertical layers up to 9 km should provide a reasonable estimate of the tropospheric NO_2 column, as the majority of NO_2 is contained within this altitude range.

The simulations followed a one-way nesting approach with 3 nested domains. The parent domain covered Europe (15°W-35°E; 35-70°N), the intermediate domain focused on North-western Europe (2-16°E; 47-56°N), and the target domain covered the Netherlands (3.1-7.5°E; 50.3-53.7°N) with a horizontal resolution of 2x2 km^2. The model was run using the European Center for Medium-Range Weather Forecast (ECMWF) Integrated Forecast System (IFS) as the meteorological driver. The emissions used at the European scale were taken from the CAMS-REG-v5.1 inventory, whereas the emissions for the Netherlands domain were a combination of the CAMS-REG-v5.1 inventory, with the Dutch and German emissions replaced by the national GrETa and ER emission inventories (in both cases using reported emissions of 2018). The emission inventories previously mentioned consist of annual total estimates, which were distributed using monthly, daily, and hourly time factors for different aggregated source categories. Emissions are also distributed vertically, with specific heights assigned on a sector-by-sector basis. In particular, industrial sources and public power stations have vertical distributions based on typical average stack heights. Further details can be found in Manders et al. (2021).

Two types of synthetic datasets were derived from the modeling outputs. (1) A synthetic dataset at the native CTM resolution and grid, temporally interpolated to 13:30 LT to align with TROPOMI's overpass time, and (2) a synthetic dataset of NO_2 VCD spatiotemporally interpolated into the TROPOMI grid and timestamp for each of the orbits that crossed the Netherlands during the period of analysis, and excluding the pixels where and when TROPOMI observations do not satisfy a quality assurance value over 0.75. Figure 1 shows the different types of datasets, demonstrating the variation in resolution and the absence of valid data in the synthetic dataset at the TROPOMI grid, where clouds and problematic retrievals occurred.

We compared LOTOS-EUROS synthetic NO_2 VCD with TROPOMI daily observations, finding good agreement in the shape, direction, and extent of plumes for major hotspots in the Netherlands, North Belgium, and West Germany. Figure A1 illustrates two examples of these comparisons. The high-resolution simulations of our simulations oversample TROPOMI's resolution by a factor of two, providing a more detailed representation of the chemistry within the plumes.

2.3 Meteorological and chemical inputs for the FDA

Temperature, planetary boundary layer (PBL) height, and zonal and meridional components of the wind at various vertical levels were extracted from the LOTOS-EUROS meteorological files, which were regridded from ECMWF-IFS operational forecast data. Only the data that was downscaled to the innermost nested domain was used to have high-resolution information (2x2 km^2). In addition, OH concentrations at various vertical levels and NO VCDs were extracted from the LOTOS-EUROS outputs.

3 Methods

3.1 Emissions estimation using the flux divergence method

Following the implementation of the steady-state continuity equation proposed by Beirle et al. (2019),

$$E = D + S = \nabla(LV\mathbf{w}) + \frac{LV}{\tau} \tag{1}$$

where the $\mathrm{NO_x}$ emissions (E) are computed as the sum of the divergence of the $\mathrm{NO_x}$ flux (D) and a sink term (S). The $\mathrm{NO_x}$ flux can be expressed as $LV\mathbf{w}$, where V is the tropospheric $\mathrm{NO_2}$ VCD observation, L is a conversion factor from $\mathrm{NO_2}$ to $\mathrm{NO_x}$, and $\mathbf{w}$ represents the wind field. The sink term S can be represented as LV/τ, where τ is the lifetime of $\mathrm{NO_2}$ at overpass time. The lifetime depends on the rate of loss of $\mathrm{NO_x}$, which can occur through chemical reactions, deposition, and dispersion (Griffin et al., 2021). However, during daylight, the primary mechanism for $\mathrm{NO_x}$ loss is its chemical reaction with hydroxyl radicals (OH), resulting in the formation of nitric acid ($\mathrm{HNO_3}$) (Lange et al., 2022).

The divergence term $\nabla(LVw)$ can be estimated on a grid using a fourth-order central-finite difference,

$$\nabla\mathbf{f}(x) = \frac{f(x-2h) - 8f(x-h) + 8f(x+h) - f(x+2h)}{12h}, \tag{2}$$

where *f(x)* represents *LVw* and h is the spacing between observations. Note that other finite difference methods can be used. As part of the preliminary test conducted on this study, a second-order method including the nearest neighbors in the east-west and north-south directions, and a second order including the neighbors in the diagonal direction were conducted. The impact of changing the finite difference scheme was minor, within 0,5% for normalized bias and gross error, and 0,02 in correlation. Koene et al. (2024) recommend calculating the divergence term using the smallest possible stencil to reduce noise impact. Consequently, applying a second-order finite difference method or estimating flux at cell boundaries might be more effective when processing noisy data. However, these improvements were not discernible in this study, as the synthetic $\mathrm{NO_2}$ fields used are noise-free. All reported results below are based on the fourth-order approach, to keep consistency with the original implementation of the FDA. Further details on the assumptions or methods used to select all the variables discussed previously are presented below.

3.1.1 Steady-state assumption

The steady-state assumptions imply the absence of accumulation or depletion of atmospheric NO_x concentrations within the analyzed area. Factors such as turbulent mixing, changes in wind patterns, variations in emission sources, and sinks can disturb this balance and create fluctuations of NO_x within the plumes (Koene et al., 2024). However, when averaged over time and across different realizations of the turbulence, the influence of these variations can be reduced. For instruments like TROPOMI, stability in typical overpass conditions is assumed. Indeed, Li et al. (2021) examined the daily variation of NO_2 and demonstrated that during the period from 12:00 to 14:00, NO_x emissions and mixing layer heights exhibit comparable levels, resulting in stable NO_2 concentrations, which support the assumption of a steady state during/around the overpass of TROPOMI.

3.1.2 Wind fields

The application of the FDA requires the reduction of the three-dimensional transport of pollutants in the atmosphere into a two-dimensional space, involving the estimation of effective zonal and meridional wind fields (or along and across track when using satellite grids directly). These effective wind components should be profile-weighted, which requires prior knowledge of the NO_2 and wind profiles within the column (Koene et al., 2024). As an approximation, Lorente et al. (2019) used NO_2 weighted and unweighted mean boundary layer wind fields, while Bryan (2022) proposed to dynamically extract the wind components based on a specific fraction of the PBL (half PBL height), which works well under the assumption of well-mixed NO_2 within the PBL. Alternatively, some authors proposed using a fixed altitude below the PBL height at the time of the satellite overpass, such as 450 m (Beirle et al., 2019), 300 m (Beirle et al., 2021), 100 m (de Foy et al., 2022; Goldberg et al., 2022) and 80 m (Misra et al., 2021). Nonetheless, this approach neglects the day-to-day variability and spatial patterns of the PBL, affecting the NO_2 and winds vertical distribution within the columns.

The wind divergence becomes non-zero when more air leaves a vertical column than enters it, and it is a phenomenon induced by global-scale processes (such as vertical transport and transport between high and low-pressure areas), large-scale features (like mountains and coastlines), and due to numerical interpolation (Bryan, 2022). Moreover, simplifying the three-dimensional structure into a two-dimensional representation on the FDA leads to a violation of the conservation of air mass. It is therefore important to address wind divergence effects. Removing the divergence from the 2D wind field ensures that the air mass of the 2D total column field is locally conserved. Bryan (2022) outlined an iterative algorithm to generate a wind dataset with reduced divergence by making slight adjustments to the wind fields. The method is similar to the Newton-Rhapson technique which iteratively approximates the minimum of a function by descending along the gradient of the function. For a comprehensive description of the method, readers are directed to the study by Bryan (2022)

3.1.3 NO_2 lifetime (τ)

During satellite overpass time (13:30 LT for TROPOMI), the main mechanism for NO_x chemical loss is the reaction of NO_2 with OH to form HNO_3.

$$OH + NO_2 + M \rightarrow HNO_3 + M \quad \text{(R1)}$$

This reaction is characterized by a lifetime τ, and in its original implementation, Beirle et al. (2019) used a constant τ of 4 hours to estimate NO_x emissions in Riyadh, South Africa, and Germany. This value was derived from the analysis of the downwind plume from Riyadh and generalized as an average representative value of the NO_2 decay from megacities and power plants as observed from satellite instruments. However, this approach neglects the nonlinear dependency between τ and NO_x concentrations (Laughner and Cohen, 2019; Valin et al., 2013), as well as the dependency on the photolysis rate, temperature, and relative humidity (Beirle et al., 2003; Misra et al., 2021). To address this complexity, a recent study (Rey-Pommier et al., 2022) has employed a first-order kinetic equation to represent the rate constant for the reaction R1,

$$\tau = \frac{1}{K[OH]} = \frac{1}{2.8e^{-11}\left(\frac{T}{300}\right)^{-1.3}[OH]}, \quad (3)$$

where τ is computed from temperature (T [K]) and the OH concentration (OH in $\mathrm{molecules\ cm^{-3}}$]). In Rey-Pommier et al. (2022) OH was extracted from global model simulations by CAMS. Lifetime estimates using this method are influenced by the resolution of the CTM, owing to the nonlinear production and loss of NO_x. A CTM running at fine resolution can result in extended lifetimes in NO_x-saturated regions due to enhanced OH titration by NO_x. Conversely, in NO_x-limited regimes, it can result in shorter lifetimes as elevated VOC levels promote OH production in the presence of the available NO_X (Li et al., 2023; Krol et al., 2024).

3.1.4 NO_x deposition

Another sink for NO_x is its removal from the atmosphere through dry and wet scavenging processes. Since the application of the FDA to satellite images is limited to clear sky conditions, only dry deposition, where NO_x is directly transferred from the atmosphere to surfaces such as soil and vegetation, impacts the estimation of emissions using the FDA. However, (Rey-Pommier et al., 2022) indicated that the lifetimes associated with deposition are about an order of magnitude larger than the chemical lifetimes, making the deposition contributions to the sink less significant, as the sink is proportional to the inverse of the lifetime. Furthermore, only surface NO_x is subjected to deposition, whereas the entire column is exposed to chemical loss. In our study, we did not account for the effect of deposition on the emission inversions using the FDA. Note that this condition applies at noon when photochemistry is enhanced due to higher incoming solar radiation. At other times of the day, the contribution of deposition sinks relative to chemical sinks can become more significant.

3.1.5 NOx partitioning factor

Similarly to τ, the partition between NO and $\mathrm{NO_2}$ in the atmosphere is influenced by factors such as the actinic flux, ozone concentrations, and temperature. A constant value of $L = 1,32$ is often assumed (Beirle et al., 2019; de Foy et al., 2022; Misra et al., 2021), which is considered representative of the usual satellite observation conditions (noon time and cloud-free pixels). However, as noted by Hakkarainen et al. (2024), recent studies increasingly use model-derived values for L. This includes simulations from global models like CAMS (Lorente et al., 2019; Rey-Pommier et al., 2022) and regional models (Goldberg et al., 2022). Alternatively, Beirle et al. (2021) derived L values using a photo-stationary steady-state approach. These methods have reported L values ranging from 1,16 to 1,83, deviating from the typical mean of 1,32. Large eddy simulations (LES) further indicate that L can rise as high as 5 within the first 10 km of emitted plumes (Krol et al., 2024).

3.2 FDA test using synthetic observations

Quantifying the accuracy of FDA-derived emissions is challenging as the true emission values are unknown. An alternative approach involves conducting an end-to-end test (E2E), schematically represented in Fig 2. This entails employing synthetic satellite observations generated within a chemical transport model (LOTOS-EUROS) to assess the FDA capability to reconstruct the emissions used as input, thereby evaluating the performance of the method. Additionally, by varying the input data and configurations of the FDA it is possible to assess the sensitivity of the method and identify the setting that enhances the accuracy of the derived emissions. The specific tests conducted in this study are described below.

3.2.1 Overall performance assessment and sensitivity analyses at CTM resolution

The FDA was applied to the $\mathrm{NO_2}$ VCD synthetic observations at the native CTM resolution (2x2 $\mathrm{km^2}$) to estimate $\mathrm{NO_x}$ emissions on a daily basis, spanning from 1 June to 31 August 2018, and subsequently averaged into the three-monthly mean for June-July-August (JJA). The $\mathrm{NO_2}$ VCD at LOTOS-EUROS native resolution allows testing the FDA in ideal conditions. No quality screening is applied, ensuring full coverage of $\mathrm{NO_2}$ VCD synthetic observations (See Figure 1A). Observations are available on the model grid, avoiding interpolations in the observation operator, and the kernels are idealized as unit vector (1,1,..,1) so the observations correspond to true total columns.

Seven tests, summarized in Table 1, were conducted to assess the FDA's overall performance and examine its sensitivity to different input data and configurations. Tests 01 and 02 were conducted to evaluate the impact of using the full LOTOS-EUROS modeled column versus only the column within the PBL as a more accurate proxy for representing instantaneous emissions at satellite overpass time. Under typical noon conditions, which correspond to the TROPOMI overpass time, emissions are generally contained within the PBL. Therefore we consider using PBL-integrated columns to be a valid approach. However, in the early morning, when the PBL is still forming, some emissions may extend beyond the PBL, a phenomenon that is prone to occurring only during winter periods. To the best of our knowledge, applications of the FDA approach in the peer-reviewed literature have exclusively used $\mathrm{NO_2}$ tropospheric columns without critically considering that free tropospheric $\mathrm{NO_2}$ is decoupled from surface emissions. Liu et al. (2021) excluded the free tropospheric contribution in their analysis of methane

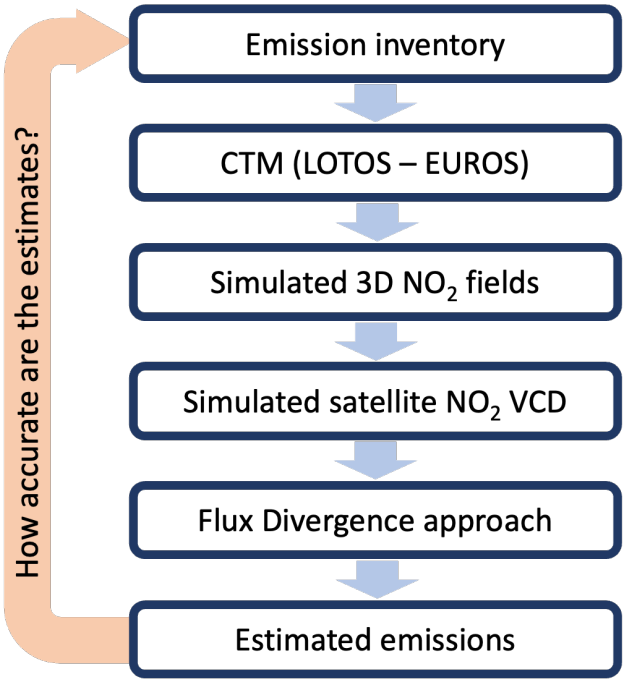

Figure 2. Schematic representation of the evaluation system designed to assess the accuracy of the NO_x emissions derived using the flux divergence approach

emissions, while Hakkarainen et al. (2022) applied a similar approach for CO_2. Tests 02-05 assessed the impact of using different fixed-altitude wind fields compared to dynamically selected wind fields based on PBL height. After identifying the optimal approach for selecting wind fields, Test ID06 evaluated the impact of using dynamic lifetimes and NO_2 to NO_x conversion values derived from the LOTOS-EUROS simulation as opposed to fixed-single values. Finally, Test ID07 assessed the impact of wind fields corrected for divergence on the final emission estimates.

The accuracy in each scenario was evaluated qualitatively, through comparisons between the JJA emissions map for the original and derived emissions at 13:30 LT, and quantitatively, computing statistical metrics such as correlation coefficient (R), normalized mean bias (NMB), and normalized mean gross error (NMGE). These metrics were calculated at the pixel level for the entire simulated domain and for the hotspot subset separately, defined as pixels containing the top 10% percentile emission values of the original emission inventory. Detailed definitions of these statistical metrics can be found in Appendix A.

A second set of performance metrics was estimated by comparing the FDA-derived emissions with a convoluted version of the model-ingested emissions, using a 3x3 grid cell spread function of the form ([1/16, 1/8, 1/16], [1/8, 1/4, 1/8], [1/16, 1/8, 1/16]). This convolution spreads the original emissions into neighboring cells, mimicking the numerical smearing caused by the numerical solution of the divergence term in the FDA, enabling a more fair comparison between datasets. With this kernel a point emission is effectively distributed over 4 grid cells. Figure 3 shows the original and convoluted model-ingested emissions alongside the FDA-derived emissions in Test ID06, illustrating how the datasets compare in each scenario. When compared to

Table 1. Summary of sensitivity tests applied using the NO_2 VCD at native model resolution.

ID	Column integration height	Winds altitude	Lifetime	NO_x/NO_2	Divergence-free winds
01	Troposphere	250 m	4 h	1,32	No
02	PBL	250 m	4 h	1,32	No
03	PBL	500 m	4 h	1,32	No
04	PBL	750 m	4 h	1,32	No
05	PBL	1/2 PBL	4 h	1,32	No
06	PBL	1/2 PBL	Kinetic equation[a]	Modeled[b]	No
07	PBL	1/2 PBL	Kinetic equation[a]	Modeled[b]	Yes[c]

(a) Lifetime computed using Eq 3 with NO_2-weighted average values of T and OH extracted from LOTOS-EUROS for the closest simulated hour before the application of the FDA, only the vertical levels below the PBL height were used. **(b)** Values for each pixel and day using the simulated NO and NO_2 VCD from LOTOS-EUROS. **(c)** divergence-free wind dataset generated using the iterative algorithm described by Bryan (2022).

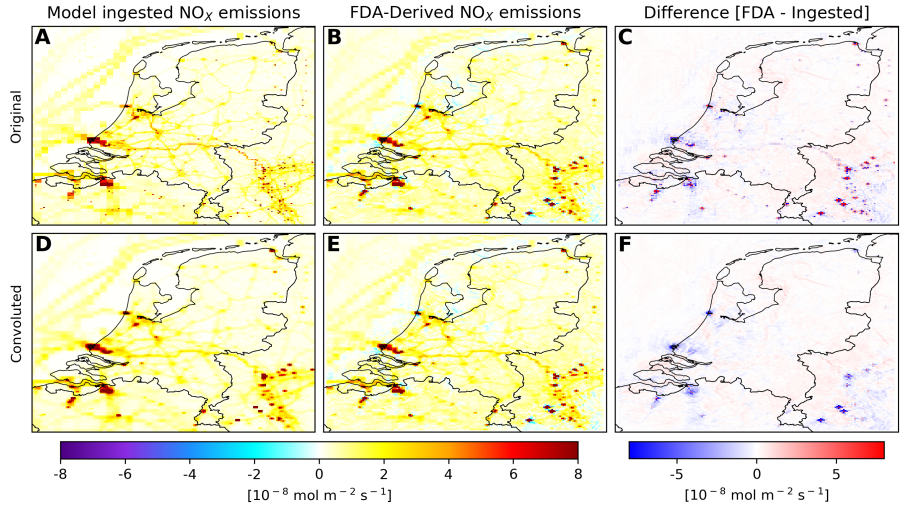

Figure 3. Comparison between the original and convoluted NO_x model-ingested emissions and FDA-derived emissions for June, July, and August (JJA), at 13:30 LT, using configuration ID06. **(A)** Original model-ingested NO_x. **(B,E)** FDA-derived NO_x. **(C)** Difference between the FDA-derived NO_x and the original ingested NO_x. **(D)** Convoluted model-ingested NO_x. **(F)** Difference between the FDA-derived NO_x and the convoluted ingested NO_x

the original ingested data, the FDA underestimate NO_x emissions for the hotspot cells and overestimate NO_x emissions at the surrounding cells (Figure 3C). However, when compared to the convoluted version of the ingested emissions, there is a better agreement between the datasets (Figure 3F).

3.2.2 Performance evaluation based on simulated TROPOMI satellite NO_2 observations

To evaluate the performance of the FDA under satellite-like observation conditions the FDA was applied using the synthetic observations at the TROPOMI grid. This includes coarser horizontal resolution, the actual TROPOMI irregular tilted push-broom observation grid, and missing pixels due to clouds using the TROPOMI qa_value flag. Note that these are idealized observations because no observation noise was added. For this evaluation, the wind fields, lifetime, and the NO_2 to NO_x conversion factor were selected based on the configuration that demonstrated optimal performance (minimizing NMB and NMGE) during the sensitivity analyses conducted in the preceding stage of this research.

3.2.3 Evaluations with real TROPOMI data

Finally, the FDA was used on real TROPOMI data, employing both the default TM5-MP NO_2 *a-priori* profile shape and the updated LOTOS-EUROS NO_2 profile, to assess the influence of the profile shape used in the retrieval on the emission estimate. Once more, the selection of wind fields, lifetime, and the NO_2 to NO_x conversion factors were determined based on the best scenario identified during the sensitivity analyses.

3.3 Spatiotemporal interpolations and other data-processing considerations

Temporal interpolations for the various variables were conducted linearly using the two nearest simulated hours to the desired timestamp. Similarly, wind vertical interpolation followed a linear approach, considering the two nearest vertical levels of the LOTOS-EUROS model to the desired altitude. Chemical fields (NO, NO_2, and OH) were horizontally regridded when necessary using a conservative interpolation method, while meteorological fields (winds, PBL height, and temperature) were regridded using a bilinear interpolation method. We made use of the xESMF library (Zhuang et al., 2023) within the Python programming language.

To apply the FDA using synthetic observations at the TROPOMI grid alongside actual TROPOMI data, divergence and emissions are estimated on a tilted irregular grid for each orbit. Subsequently, the emissions are regridded into a regular 5x5 km array to facilitate averaging into the JJA mean emissions, utilizing the conservative interpolation method of xESMF once again. It is important to note that estimating the divergence on the TROPOMI grid requires the rotation of the wind fields from a east-west and north-south components into across-track and along-track components.

4 Results and discussion

4.1 FDA performance for model grid observations

The FDA was implemented in seven different experiments listed in Table 1. The performance evaluations, summarized in Table 2 and Figure 4, indicate that experiment ID06 offers the best NMB values for the entire domain (3,2%), low NMB over hotspot regions (-8,6%), and a standard deviation that aligns closely with the convoluted emissions input into LOTOS-EUROS. This indicates improved accuracy in capturing the variability of the JJA prior NO_x emissions. Therefore, the results of the test ID06

Table 2. Performance metrics using the synthetic observations at LOTOS-EUROS grid

ID	Total emissions [a]	Original ingested emissions						Convoluted ingested emissions					
		Entire domain			Hotspots			Entire domain			Hotspots		
		NMB	NMGE	R	NMB	NMGE	R	NMB	NMGE	R	NMB	NMGE	R
01	981,7	59,0	98,6	0,71	-8,6	46,4	0,86	59,0	74,4	0,95	16,5	25,9	0,98
02	567,8	-8,0	63,2	0,74	-35,9	47,8	0,87	-8,0	42,1	0,95	-18,3	23,9	0,98
03	589,7	-4,5	61,0	0,75	-32,6	46,1	0,88	-4,5	38,9	0,96	-14,0	21,5	0,98
04	592,8	-4,0	63,4	0,75	-31,7	46,8	0,89	-4,0	41,2	0,96	-12,9	22,5	0,97
05	589,6	-4,5	60,4	0,76	-31,6	45,3	0,89	-4,5	37,8	0,97	-12,8	20,0	0,98
06	636,8	3,2	63,2	0,80	-28,3	43,7	0,92	3,2	42,3	0,94	-8,6	22,3	0,96
07	638,8	3,5	61,8	0,80	-28,8	43,7	0,92	3,5	41,0	0,94	-9,2	22,3	0,96

(a) FDA-derived NO_x aggregated emissions for the entire simulation domain in mol s^{-1}. Total *a-priori* NO_x emissions used as input in LOTOS-EUROS were 617.4 mol s^{-1}.

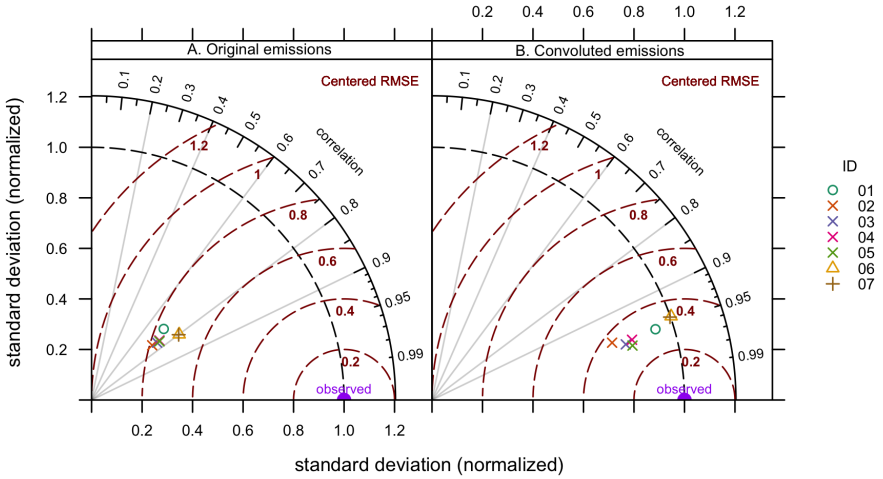

Figure 4. Taylor diagram summarizing the FDA performance for the seven sensitivity test of table 1 with ID 01 to 07 using **(A)** the original model-ingested emissions and **(B)** convoluted model-ingested emissions as a reference

are used as a benchmark for the following discussion. Note that test ID07, where the wind divergence is mitigated, achieves similar performance metrics.

Fig 5 compares the JJA mean NO_x emissions ingested into LOTOS-EUROS and those derived with the FDA. Overall, the FDA effectively reconstructs the spatial distribution of emissions, capturing major industrial and urban sources such as the port of Rotterdam, the city of Amsterdam, and Schiphol Airport. Moreover, the FDA captures minor emission sources, exemplified by the retrieved emission in the road network, inland shipping along the Rhine River, and small hotspots in Den Helder, Leeuwarden, and Groningen, located in the northern region of the Netherlands.

Despite the good correspondence in spatial distribution, the FDA spread out the emission hotspots to neighboring grid cells, particularly evident in the Ruhr area. This is caused by numerical smearing which induces an underestimation of emissions at the hotspots, misallocating part of the emissions to neighboring cells (Cooper et al., 2017). This smearing arises from the numerical solution of the divergence term which is unable to represent sharp fluctuations with a size of the order of a single grid box. The fourth-order central-finite difference employed in this research incorporates data from adjacent grid cells in both east-west and north-south directions, thereby smoothing the divergence term. The smearing effect may also result from biases in the CTM-predicted NO_2 fields due to numerical diffusion when resolving the advection equation at the model grid, which artificially smooths the solution in regions with steep concentration gradients, leading to plume stretching (Eastham and Jacob, 2017; Rastigejev et al., 2010).

The impact of pollutant transport on emission smearing was not discernible in the findings of this study. Figure A2 illustrates emission maps grouped by days predominantly experiencing northerly and southerly winds. Emissions exhibit smearing in all directions surrounding the hotspots, attributed to the aforementioned numerical effects, rather than being primarily directed towards cells in the downwind direction. TROPOMI measures NO_2, which is not immediately formed at the source, but only after the reaction of NO with O_3 has taken place. Consequently, a displacement downwind of the source location occurs as NO converts into NO_2 and becomes visible to the satellite. This did not occur in the synthetic experiments presented here because the NO_2 to NO_x ratio was derived from modeling outputs, ensuring that all atmospheric NO_x was included.

Regarding total emission values, the FDA underestimates emissions in hotspot areas, with an average NMB of -8,6%. This discrepancy is primarily due to the smearing effect previously discussed, which is not entirely corrected when compared to the convoluted emissions ingested by the model. Furthermore, inaccuracies in representing the lifetime of NO_x will contribute to the bias. Indeed, the modeled OH concentrations, used in Eq 3, are highly uncertain due to their numerous sinks, rapid cycling, and nonlinear chemical feedbacks. Discrepancies in OH simulations across different models can be considerable, as shown in Figure A3, owing to differences in photolysis rates, cloud parameterizations, radiative transfer codes, and the representation of volatile organic compounds within each model (Nicely et al., 2017, 2020). These factors collectively influence OH chemistry and, consequently, its predicted concentrations. Furthermore, OH concentrations are also affected by the resolution of the model due to nonlinear effects. Higher resolution simulations exhibit an enhanced titration of OH with NO_x in NO_x-saturated regions, leading to an extended lifetime, while having the opposite effect in NO_x-limited regions (Li et al., 2023; Krol et al., 2024). In contrast to the hotspots, the FDA slightly overestimates background emissions (NMB of 3,2%). This is mainly associated with biases in the lifetime estimation. Likewise, negative emission values may occur due to biases in the chosen wind fields, affecting the estimation of divergence.

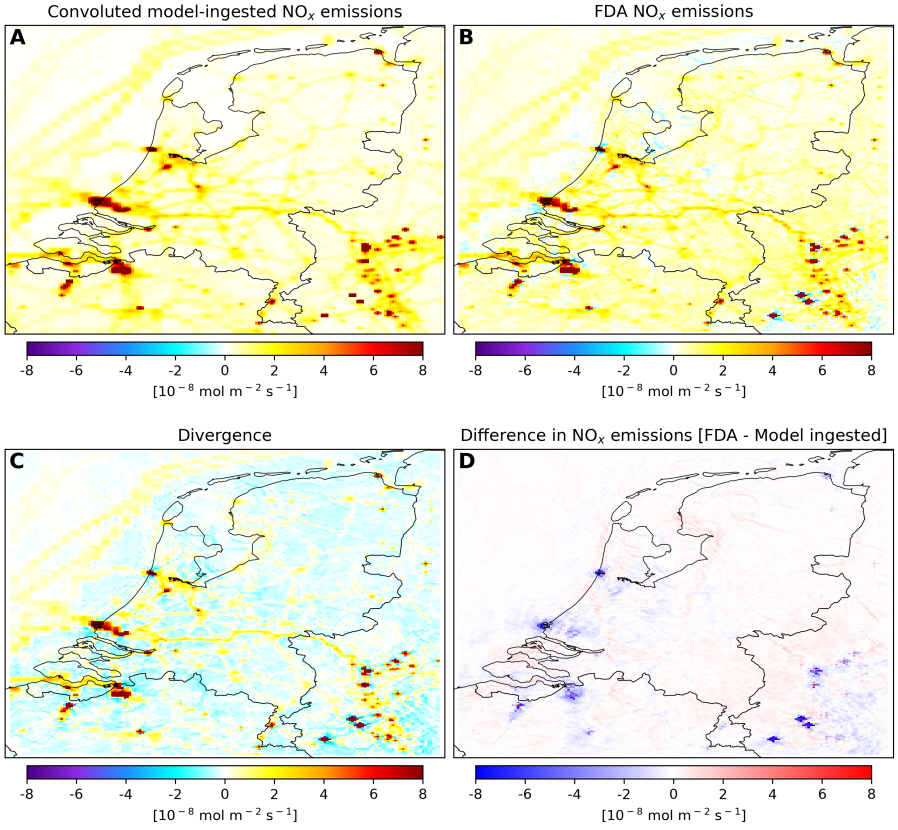

Figure 5. Mean NO_x emissions and divergence for June, July, and August (JJA) at 13:30 LT derived from the synthetic dataset at LOTOS-EUROS native resolution using configuration ID06. **(A)** Convoluted NO_x emissions ingested into LOTOS-EUROS. **(B)** FDA-derived NO_x emissions. **(C)** NO_x flux divergence. **(D)** Difference in NO_x emissions between the FDA-derived dataset and the convoluted model-ingested emissions.

In summary, the FDA demonstrates a good performance in reconstructing the spatial pattern of emissions and maintaining a low bias in hotspot areas provided that wind, τ, and the NO_2 to NO_x conversion factors are known to good accuracy.

4.1.1 Column integration height

Experiments ID01 and ID02 examine the effect of the integration height of the NO_2 column used for emission calculations. This test has the most significant impact on the overall results. Using the full modeled tropospheric column (Test ID01) results in an overestimation of emissions by 59% across the entire domain. In contrast, integrating the column only up to the PBL height leads to a slight underestimation of -8%. The integration height of the column primarily affects the sink term in equation 1, as it is directly proportional to the NO_x column. Using the full tropospheric column leads to a significant overestimation because residual NO_x from long-range transport above the PBL top or entrainment with the upper boundary conditions of

the simulation is included. According to our simulations, the free tropospheric NO_2 can represent between 20 to 65% of the column. This residual NO_x has no direct relation to the instantaneous emissions being evaluated at the time the FDA is applied. Additionally, the PBL and free tropospheric NO_2 are exposed to different chemical sinks. Thus, using a single lifetime value of 4 hours may not accurately represent the entire tropospheric column.

The residual NO_2 column obtained after subtracting the PBL contribution (See Figure A4), still exhibits significant concentrations over the Ruhr area, Antwerp, and along the Dutch coastline. These regions contain the majority of NO_x emissions, suggesting that the spatial patterns in the residual layer may reflect enhancements in the free troposphere caused by emissions from previous hours. The high concentration in the residual layer can also originate because the PBL does not align precisely with the model layer interfaces, leaving part of the column excluded from the inversion process. This can partially explain the low negative bias of -8% when deriving emissions using this approach.

A similar approach was impelementend by Liu et al. (2021), who used the FDA to derive methane emissions. In their study, they used a PBL column of methane and validated this approach against GEOS-Chem outputs. Their validation also demonstrated improved performance of the FDA, as using a PBL column excludes transport in the upper troposphere. Furthermore, Koene et al. (2024) noted that removing background fields is advantageous because it allows the analysis of wind fields to be confined to the PBL rather than the entire column, and also eliminates the need to make assumptions about the steady-state conditions for the background field.

4.1.2 Wind fields

Experiments from ID02 to ID05 were conducted with all variables held constant, except for varying the altitude of the chosen 2D wind field. The results of these experiments show similar performance in reproducing the original emission dataset. The total emissions obtained differ only by 4% and correlation and NMGE exhibit comparable values, as summarized in Table 2. Additionally, the mean divergence maps, depicted in Fig A5, reveal close agreement regardless of the chosen wind altitude. These results may be specific to the study area, given the uniformity of wind patterns in the Netherlands due to the flat terrain. Indeed, as depicted in Figure A6, wind speed and direction over land exhibit minimal variations with altitude, with the primary distinction being an increase in wind speed near the Netherlands coast when using the half PBL height for selecting the wind fields. Application of the FDA in areas with more complex orography may require additional investigation into selecting the optimal wind height.

Despite the observed similarities, it is still advisable to dynamically select the wind field altitude as a function of the PBL to capture its day-to-day variability and spatial patterns such as contrasts between land and sea. As demonstrated in Fig A7, this variability is evident, with PBL values fluctuating between altitudes lower than 100 m and higher than 1500 m. In this study, using a half PBL altitude for the wind fields provided the best metrics for NMB (-12,8%), NMGE (20,0%), and correlation (0,98) for the hotspots in comparison to the fixed wind altitude alternatives.

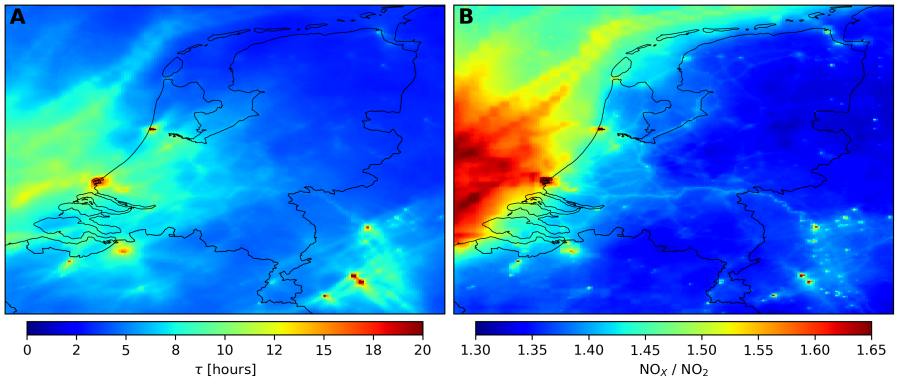

Figure 6. Mean NO_2 lifetime (τ) and NO_x to NO_2 (L) for June, July, and August (JJA) derived from LOTOS-EUROS simulation, at 13:30 LT. **(A)** Mean PBL NO_2-weighted τ determined using Equation 3, employing average values of temperature (T) and hydroxyl radical (OH) from LOTOS-EUROS for the two hours immediately preceding the application of the FDA. **(B)** Mean L, determined by the ratio between vertical column densities of NO_x and NO_2 from LOTOS-EUROS

4.1.3 NO_2 lifetime and NO_2 to NO_x conversion factor

Using a lifetime derived from OH and T and a NO_2 to NO_x conversion factor from the LOTOS-EUROS simulation (Test ID06) yields notable enhancements compared to employing single fixed values across the entire period and domain (Test ID05). Specifically, this approach diminishes the underestimation over hotspot regions (-8,6% vs -12,8%), and improves the bias over the entire domain in general (3,2% vs -4,5%). Furthermore, the normalized standard deviation depicted in Figure 4, indicates that the variability of the derived emissions with this method more closely matches the variability of the *a-priori* NO_x emissions ingested in LOTOS-EUROS. Note that while the results using a fixed lifetime of 4 h are still acceptable, the method heavily depends on the assumed value. For example, changing the assumed value to 5 h would increase background underestimations to -20%, whereas using 3 h would result in an overestimation of 22%.

The mean lifetime map, shown in Figure 6A, reveals a strong spatial variability at the spatial resolution of the model. In areas with high emission levels, lifetimes surpass 20 hours, reflecting the low local OH concentrations. Similarly, lifetimes over the North Sea range from 8 to 14 hours, also due to a reduced availability of OH which is depleted with fresh shipping emissions. Both scenarios show a substantial departure from the 4-hour estimate cited by Beirle et al. (2019). In the North-East part of the Netherlands however, emission density is lower and the lifetime becomes closer to the 4-hour value. Using modeling-derived lifetime better represents ageing of the pollution plumes. Figure A8 shows that the NO_2 lifetime reaches its maximum over the concentration hotspots and gradually decreases downwind according to LOTOS-EUROS. At the emission source, the lifetime peak due to local titration of OH, which is recovered downwind as the plume mixes with fresh air (Krol et al., 2024; Vinken et al., 2011). Considering the spatiotemporal variability of the NO_2 lifetime contributes to a more precise reconstruction of the original emissions in comparison to using a single lifetime value.

Due to the long lifetimes at the hotspots, the contribution of the S term in Eq 1 becomes small, thus making D the dominant factor for retrieving emissions at the hotspot location. On the contrary, for retrieving emissions at the country level or the entire simulation domain, the sink term is the dominating factor for estimating emissions. Indeed, if the net inflow or outflow of pollutants across the boundaries is negligible, the D term becomes zero. Consequently, emissions are dominated by S, which is proportional to $1/\tau$, so a bias in τ will directly result in a bias in the total emission. This aspect represents a drawback of the method due to the considerable uncertainty of this parameter.

The complexities involved in estimating lifetimes are not unique to the FDA. Model-derived lifetimes, based on OH availability, can be biased, as previously discussed in Section 4.1. Alternative methods for deriving lifetimes include the simultaneous estimation of emissions and lifetimes using downwind NO_2 patterns derived from the satellite observations directly. This approach reduces reliance on prior assumptions or model-based inputs and is applied in plume dispersion methods to estimate emissions from single (Beirle et al., 2011; Valin et al., 2013) or multiple sources (Fioletov et al., 2022; Dammers et al., 2024). However, this method is not always feasible, as plumes are not always isolated and cannot always be idealized as point sources. Additionally, covariance between emissions and lifetimes introduces errors into lifetime estimations.

Figure 6B illustrates the mean NO_x to NO_2 ratio simulated by LOTOS-EUROS. Deviations from the value of 1,32 proposed by Beirle et al. (2019) manifest prominently over concentration hotspots, the North Sea, and adjacent coastal regions, where elevated ratios reaching up to 1,60 are obtained. The higher ratios over the hotspot areas are caused by the proximity to large concentrations of freshly emitted NO, leading to local titration of O_3; hence, reducing the reactions to form NO_2. Similarly, the presence of ship emissions over the North Sea and coastal regions, along with a shallower boundary layer compared to inland areas, contributes to the reduction of O_3 in the marine boundary layer and accounts for the high ratios.

As previously discussed for the lifetime, deriving a NO_2 to NO_x conversion factor from simulation outputs can be advantageous for estimating emissions over extended periods. Alterations in atmospheric chemical processes, driven by different emission scenarios, can influence the non-linear relationship between NO_x and O_3, thereby altering the NO_x to NO_2 ratio. In the Netherlands scenario, Zara et al. (2021) observed a decrease in NO-titration from 2005 to 2018 due to lower NO_x emissions, causing a shift in the NO–NO_2 equilibrium towards higher concentrations of NO_2. This led to the reductions in the surface air NO_x to NO_2 ratio during winter (from 1,45 to 1,28) and summer seasons (from 1,30 to 1,20).

4.1.4 Divergence-free winds

For the period and domain used in this study, a large-scale wind divergence primarily manifests along the coastline, as exemplified in Figure A9. The iterative algorithm used to mitigate the wind divergence in the dataset (Bryan, 2022) successfully diminishes it, without substantially altering the wind patterns. Using these divergence-free wind datasets (Test ID07) does not substantially change the retrieved emissions, resulting in only a slight reduction in the NMGE (42,3% vs. 41,0%) for the entire domain. The other performance metrics remain almost identical, indicating that the impact of wind divergence in the domain and period studied is small. The small effect of reducing the wind divergence term in our findings is due to our integration of NO_2 VCD only up to the PBL height. As noted by Koene et al. (2024), addressing the wind divergence term can be beneficial when the background is not been subtracted from the columns.

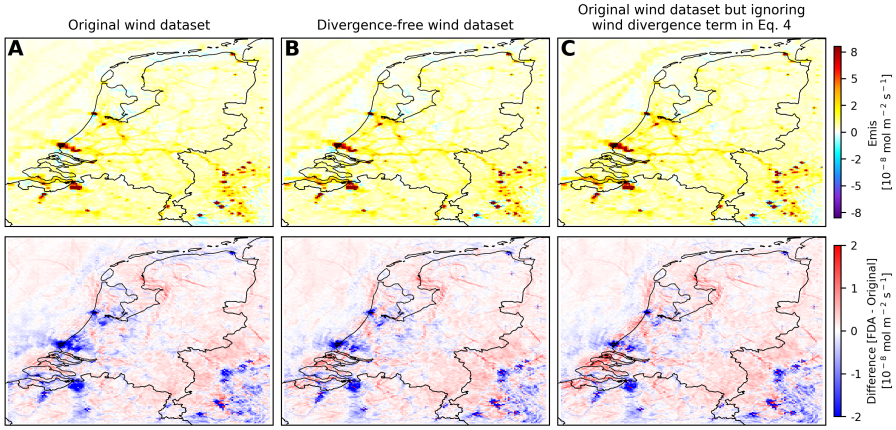

Figure 7. Comparison of mean NO_x emissions for June, July, and August (JJA) at 13:30 LT derived from the synthetic dataset at LOTOS-EUROS native resolution using the **(A)** original wind dataset, **(B)** the divergence-free wind dataset, and **(C)** original wind dataset but skipping the divergence term in Eq 4, and difference map between the derived FDA-emissions and the emissions originally ingested into LOTOS-EUROS.

Note that the flux divergence in Eq 1 can be expanded using the product rule into advection and wind divergence terms,

$$D = \nabla(LV\mathbf{w}) = \mathbf{w} \cdot \nabla(LV) + LV \cdot \nabla(\mathbf{w}) \tag{4}$$

Beirle et al. (2023) suggested omitting the wind divergence term, arguing that its influence is insignificantly small for D. However, Figure 7C, shows that by excluding the divergence term in Eq 4 there is an increased emission overestimation at the coastline.

4.1.5 Application of the FDA for other times of the day

In addition to the TROPOMI overpass time test, two additional scenarios were examined at 08:00 and 18:00 LT. This was conducted to gain insights into the applicability of the FDA beyond stable conditions, which could have implications for employing the method to derive emissions from geostationary satellites such as GEMS, TEMPO, and the upcoming Sentinel-4 sensor. The same experimental settings as in ID06 were employed for this assessment.

Figure 8 shows the derived emission and divergence maps for the scenarios above. At 08:00 LT, the emissions and divergence map are almost equal. A low concentration of OH during this period leads to significantly longer lifetimes computed with Eq 3, thus the sink term in the Eq 1 becomes negligible. This leads to extensive negative emission areas, as revealed in Figure 8B. These errors mainly stem from ignoring the accumulation of atmospheric NO_x during non-stable conditions, within a PBL in development and with changing emissions. Therefore, deviating from the steady-state assumption in the FDA. Additionally, because the chemical lifetime is significantly extended due to reduced photochemistry at this time, the sinks due to deposition, previously unaccounted, may become more significant and need to be included to compensate for the negative emission artifacts.

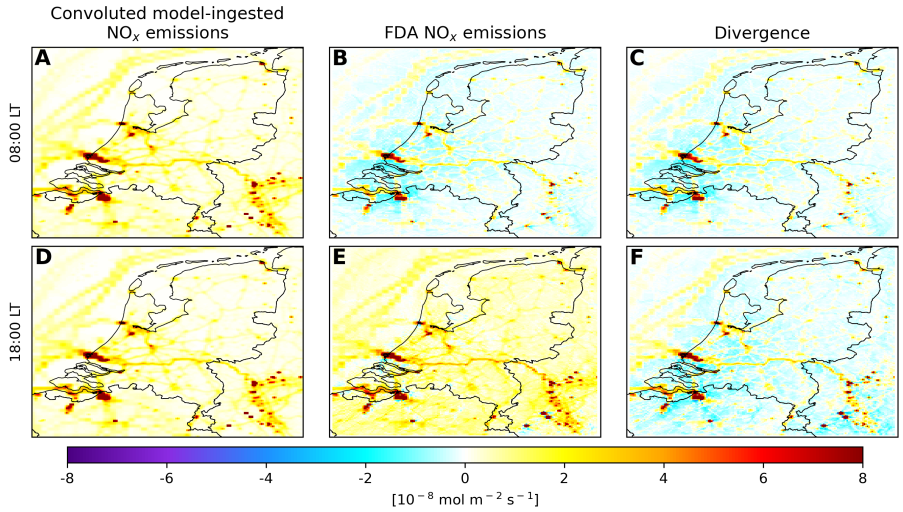

Figure 8. Mean NO_x emissions and divergence for June, July, and August (JJA) derived from the synthetic dataset at LOTOS-EUROS native resolution using configuration ID06, at 08:00 and 18:00 LT. **(A)** Convoluted NO_x emissions ingested into LOTOS-EUROS at 08:00 LT. **(B)** FDA-derived NO_x emissions at 08:00 LT. **(C)** NO_x flux divergence at 08:00 LT. **(D)** Original NO_x emissions ingested into LOTOS-EUROS at 18:00 LT. **(E)** FDA-derived NO_x emissions at 18:00 LT. **(F)** NO_x flux divergence at 18:00 LT.

At 18:00 LT, the emission map displays no negative artifacts (Figure 8E), but emissions are overestimated across the entire domain by 24,8% in average. The biases can be attributed to uncertainties in the diurnal variations of the lifetime and chemistry. During this time of day, photochemical processes diminish, making it necessary to consider additional competing reactions that consume OH and other sink pathways for NO_x besides the formation of HNO_3.

The diurnal profile of NO_x and NO_2 VCD within the PBL, derived from the LOTOS-EUROS simulation, undergoes distinct shifts throughout the day as shown in Fig. 9A. **(1)** During the period from 19:00 to 05:00 LT, NO_x is consumed through titration reactions with O_3, forming NO_3, which can subsequently react with another NO_2 molecule to produce N_2O_5. With low emissions of NO_x during this time, there is an insufficient supply to compensate for the consumed atmospheric NO_x, resulting in a decrease in its concentration. **(2)** Between 05:00 and 12:00 LT, there is an increase in NO_x emissions. The O_3 levels remain low following the night-time titration, which diminishes the availability of OH required to consume NO_2 and form HNO_3, consequently resulting in an accumulation of NO_x. **(3)** From 11:00 to 16:00LT, increased photochemistry and entrainment of free tropospheric O_3 into the boundary layer elevates O_3 concentrations, thereby increasing the production of OH, which subsequently consumes NO_2, leading to a reduction in NO_x. Furthermore, the PBL reaches its peak during this time, enhancing the mixing of NO_X and VOCs, which further promotes OH formation. **(4)** As the day progresses from 16:00LT to 19:00LT, photochemistry diminishes, with O_3 being primarily used in the conversion of NO to NO_2. The availability of OH to consume NO_2 decreases, resulting in the accumulation of NO_x levels.

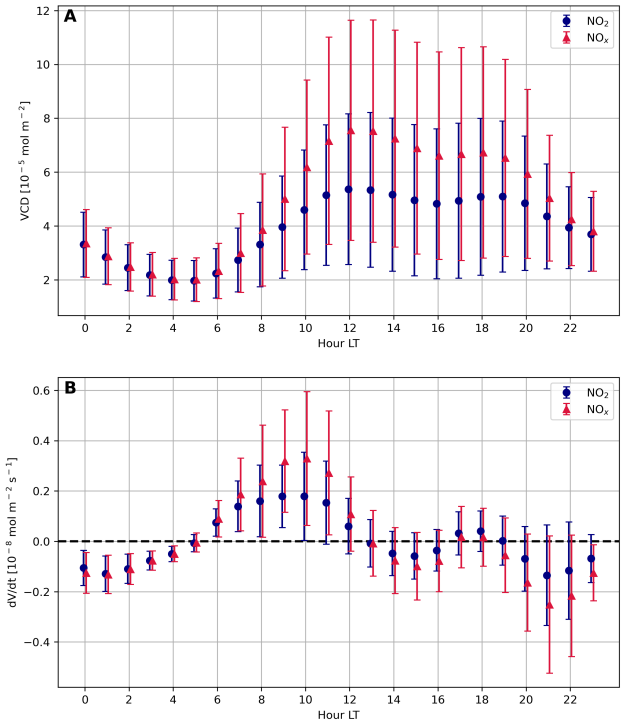

Figure 9. Mean diurnal profile for the entire simulation domain of NO_2 and NO_x vertical column densities (VCD) within the PBL for June, July, and August (JJA) derived from LOTOS-EUROS simulation **(A)**, and change rate of the VCD considering the hours i and $i-1$ **(B)**. The vertical lines represent the standard deviation of each point.

The fluctuations in NO_x VCD over time (dV/dt), as illustrated in Fig. 9B, indicate that relying on the assumption of steady-state in the FDA is insufficient at many hours of the day. Including this term will transform Eq. 1 into

$$E = D + S + \frac{dV}{dt} \tag{5}$$

thereby mitigating the underestimations observed when deriving emissions at 08:00 LT (Fig. 8B), as a positive term will be introduced to compensate for NO_x buildup. In addition, accounting for deposition-related sinks might be necessary in the early morning, as their contribution becomes significant due to the lower photochemistry during that period. It is worth noting that estimating and integrating this term is feasible in this scenario due to the availability of hourly VCD data from the simulation, and could be extended to geostationary satellite data with hourly observations. However, for polar orbit satellites like TROPOMI, evaluating this term is not viable for a single instrument, as observations are limited to just one per day. Nonetheless, it would be possible to estimate changes in NO_2 VCD using multiple polar-orbiting satellites with similar overpass times. This approach has been demonstrated by Penn and Holloway (2020) using the GOME-2 and OMI instruments, as well as by Boersma et al. (2009) using SCIAMACHY and OMI.

For the scenario at 18:00LT (Fig. 8E), incorporating the dV/dt term will not significantly affect the derived emissions as dV/dt is small at this time of the day. For an understanding of the overestimation in this scenario it is needed to reassess the lifetime estimates. This discrepancy might stem from uncertainties in the OH estimates utilized for deriving the lifetime, or it could indicate the need to incorporate additional competing reactions that consume OH and other sink pathways for NO_x, such as oxidation to produce alkyl and multifunctional nitrates (Sobanski et al., 2017; Romer Present et al., 2020). In addition, as photochemical processes diminish during this time of day, the contribution of NO_x loss due to deposition could become more significant.

4.2 FDA performance for synthetic TROPOMI observations

The accuracy of the FDA was further assessed under satellite-like observing conditions, employing synthetic observations sampled at the TROPOMI grid using TROPOMI quality screening. To conduct this evaluation, the configuration used in experiment ID06 was employed (See Table 1), as they yielded the best performance for the test conducted over the synthetic observations at the native LOTOS-EUROS grid.

The results from this test show that despite the lower resolution, irregular grid, and presence of missing pixels due to cloud cover and retrieval issues, the FDA is capable of reconstructing the spatial distribution of emissions, particularly for major emitters as shown in Figure 10. However, discerning minor emission sources like roads, inland shipping, and smaller industries proves challenging at this lower resolution. The underestimation of hotspot emissions persists for this test (NMB: -11,0%; NMGE: 18,5% with respect to the convoluted model-ingested emissions), as well as the overestimation of background regions (NMB: 17,7%; NMGE: 39,2%). These biases may be attributed to inaccuracies in the NO_x lifetime and the wind fields, as discussed previously in this study.

Note also that the generalized overestimation of the background increased from 3,2% in the synthetic observations at the model grid to 17,7% in the synthetic observations at the TROPOMI grid. This increase can partly be attributed to a sample bias, as only the pixels with cloud-free conditions are considered in this later scenario to emulate TROPOMI observations. By focusing solely on cloud-free conditions, temperature-dependent emissions in the model are amplified, impacting not only NO_x emissions but also other compounds that react with NO_x in the atmosphere, thereby affecting its lifetime. In LOTOS-EUROS, these temperature-dependant emissions include NO_x emissions from soils, biogenic VOC (also influenced by photosynthetically active radiation), and road transport emissions (Manders et al., 2021). Additionally, the increase in incoming solar radiation under cloud-free conditions enhances the photolysis of several compounds. Furthermore, the number of observations per month or pixel can vary, affecting the emissions derived from the inversion process.

4.3 Real TROPOMI data

Previous studies have shown that replacing the TROPOMI coarse TM5-MP NO_2 *a-priori* vertical profile with a high-resolution profile offers a more accurate representation of meteorological and chemical fields which increase column concentrations near emission sources by more than 30% and create a steeper concentration gradient around these areas (Laughner et al., 2016; Griffin et al., 2019; Zhao et al., 2020; Judd et al., 2020), leading to better agreement with ground-based validation (Douros

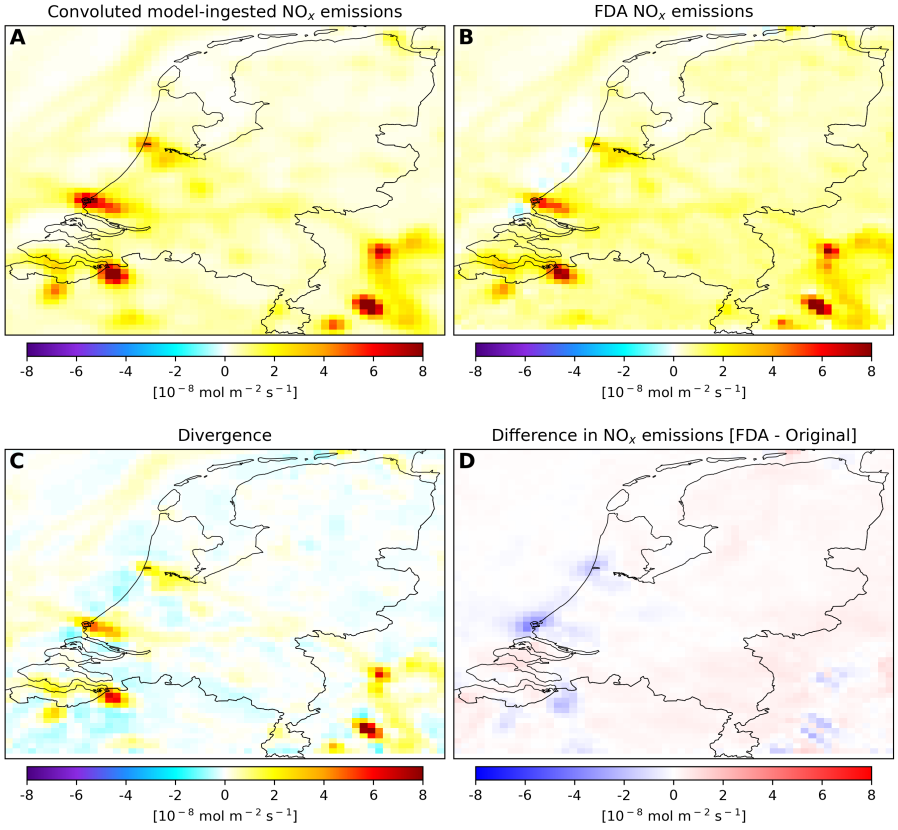

Figure 10. Mean NO_x emissions and divergence for June, July, and August (JJA) derived from the synthetic dataset sampled at TROPOMI grid and timestamp using configuration ID06. **(A)** Convoluted model-ingested NO_x emissions. **(B)** FDA-derived NO_x emissions. **(C)** NO_x flux divergence. **(D)** Difference in NO_x emissions between the FDA-derived dataset and the convoluted model-ingested emissions.

et al., 2023; Liu et al., 2020; Ialongo et al., 2020). Based on these findings, we conducted two tests using TROPOMI with the default TM5-MP NO_2 *a-priori* profile shape, and a modified version incorporating an updated LOTOS-EUROS NO_2 profile. These observations represent the total tropospheric VCD, which are subsequently converted to PBL VCD by multiplying by the ratio of PBL VCD to tropospheric VCD, as derived from LOTOS-EUROS simulations. This approach allows for a consistent methodology for real TROPOMI data, matching the one employed for the synthetic observations in experiment ID06.

Figure 11 illustrates the contrast in NO_2 VCD measurements between the TROPOMI TM5-MP product and the LOTOS-EUROS *a-priori* replacement version. The modified version of TROPOMI with LOTOS-EUROS *a-priori* exhibits notably higher NO_2 VCD values, averaging a 23% increase concerning the default TM5-MP *a-priori* product. This difference directly impacts the emission estimate, resulting in total emissions derived from TROPOMI LOTOS-EUROS being 15% higher on average, which increases to 34% when considering only the hotspot pixels. These results align with earlier research referenced previously. The updated *a-priori* profile not only enhances NO_2 vertical column densities (VCDs) at hotspot locations but also

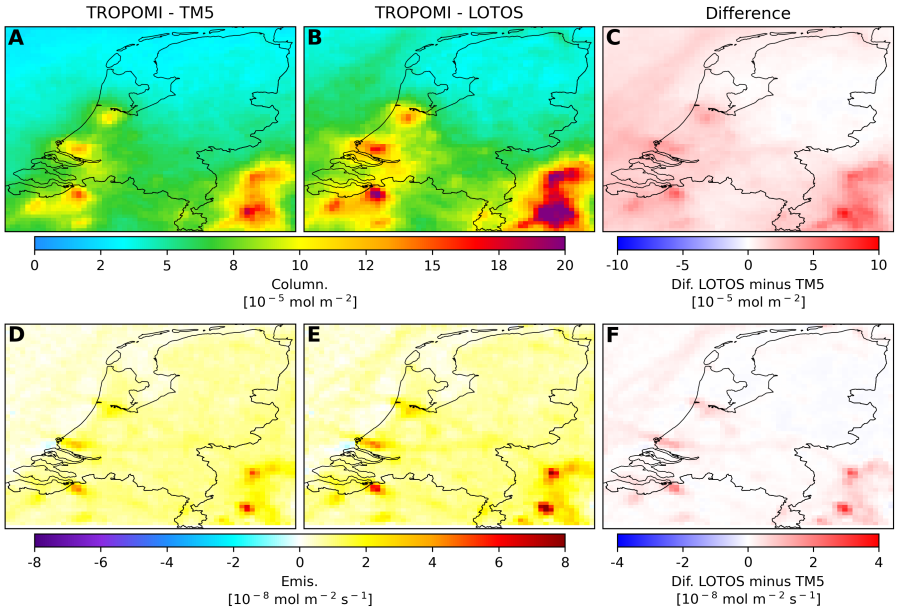

Figure 11. Mean NO_2 vertical column densities (VCD) and NO_x emissions for June, July, and August (JJA) derived using real TROPOMI data, with default TM5-MP and high-resolution *a-priori* profile shape. **(A)** TROPOMI NO_2 VCD with default TM5-MP *a-priori*. **(B)** TROPOMI NO_2 VCD with LOTOS-EUROS *a-priori*. **(C)** Difference in NO_2 VCD between TROPOMI products. **(D)** FDA-derived NO_x emissions using TROPOMI with default TM5-MP *a-priori*. **(E)** FDA-derived NO_x emissions using TROPOMI with LOTOS-EUROS *a-priori*. **(F)** Difference in NO_x emissions between TROPOMI products

provides a more accurate representation of concentration gradients, which impacts the estimation of the divergence term in the FDA (Laughner et al., 2016). Additionally, because our study uses consistent wind data for both generating the new *a-priori* profiles and calculating the divergence, we expect more accurate divergence estimates.

A comparison between the convoluted bottom-up emission inventory used in the model and the one derived using TROPOMI with LOTOS-EUROS *a-priori*, as presented in Figure 12, shows a good agreement between the datasets. The correlation coefficient is 0,83 for the entire domain and 0,79 for the hotspot areas. Using the bottom-up inventory as the baseline, TROPOMI-derived emissions are 32,2% higher for the entire domain, potentially due to TROPOMI signal issues, non-negligible accumulation terms (dV/dt), or differences in soil emissions. On the contrary, when considering only hospot areas, emissions are biased low by 18%. Applying the FDA to the synthetic data (see section 4.2) revealed an 11% negative bias at hotspot locations, indicating a general tendency of the FDA to underestimate emissions at these points. The additional 7% bias observed when using real TROPOMI data with the updated *a-priori* falls within the uncertainty ranges of both TROPOMI and bottom-up inventories.

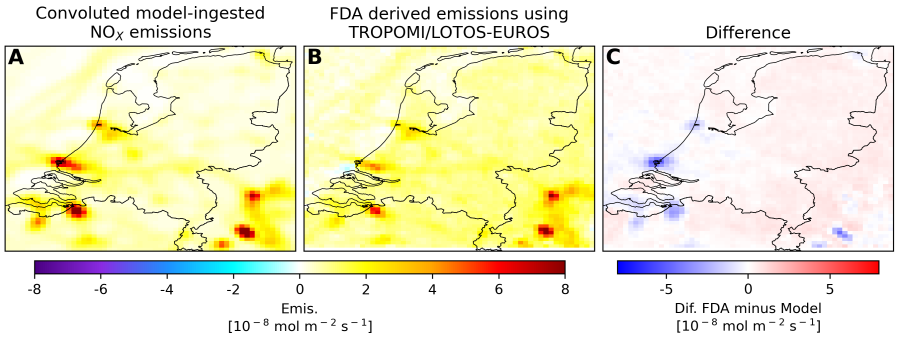

Figure 12. Mean NO_2 vertical column densities (VCD) and NO_x emissions for June, July, and August (JJA) derived using real TROPOMI data, with default TM5-MP and high-resolution *a-priori* profile shape. **(A)** Convoluted model-ingested NO_x emissions. **(B)** FDA-derived NO_x emissions using TROPOMI with LOTOS-EUROS *a-priori*. **(C)** Difference in NO_x emissions between the model-ingested and FDA-derived datasets.

4.4 General performance of the method

The application of the FDA on synthetic data at 13:30 LT demonstrates excellent results. There is a relatively low underestimation at hotspots and a slight overestimation of overall emissions for the entire domain by 3%, as summarized in Table 3. These results, however, are not achieved with the basic FDA implementation. Instead, they require the use of NO_2 VCD integrated up to PBL height, along with dynamically selected wind fields, NO_2 lifetime, and NO_2 to NO_x conversion factors. Ignoring these assumptions and relying on tropospheric VCD and fixed values for the aforementioned factors increases the generalized overestimation to an average of 59%. The favorable results with the optimal settings also suggest that the steady-state assumption at this time of day is valid, as dV/dt is sufficiently small (see Figure 9), allowing the FDA to be applied under standard noon conditions.

Conversely, when applying the FDA at different times of the day, which is necessary for handling geostationary observations, the steady-state assumption does not hold for several periods. For instance, performance using synthetic data at 08:00 LT shows extensive negative emission artifacts. This issue can be mitigated by including the dV/dt term, as suggested in Eq 5, to compensate for the depletion of atmospheric NO_x during this time. The performance of the FDA when analyzing synthetic data at 18:00 LT is significantly better, as the dV/dt term is notably small at this time of day. However, there is still an overestimation for the entire domain of 25%, which may be linked to biases in the lifetime estimation.

The FDA performance at noon using synthetic data in the actual TROPOMI grid and timestamp also shows favorable results. However, the overestimation for the general domain increases from around 3% with synthetic data at the model grid to 18% with the TROPOMI grid. It is worth noting that this latter approach has a sampling bias, as pixels with cloud coverage were removed to mimic actual TROPOMI observations. Leaving only data from clear sky conditions can induce bias as all temperature dependant emissions in the model are enhanced under these circumstances. Moreover, the number of observations per month or pixel can vary, influencing the emissions obtained from the inversion

Table 3. Summary of performance metrics using configuration ID06 for the several test made using the convoluted model-ingested emissions as a reference

Grid type	Test description	Convoluted ingested emissions					
		Entire domain			Hotspots		
		NMB	NMGE	R	NMB	NMGE	R
Model	Synthetic data at 13:30 LT	3,2	42,3	0,94	-8,6	22,3	0,96
Model	Synthetic data at 08:00 LT	-95,5	95,9	0,75	-54,3	54,5	0,79
Model	Synthetic data at 18:00 LT	24,8	48,1	0,95	2,1	20,8	0,96
TROPOMI	Synthetic data at TROPOMI timestamp	17,7	39,2	0,82	-11,0	18,5	0,91
TROPOMI	TROPOMI-TM5 *a-priori*	14,8	60,7	0,76	-39,5	40,3	0,73
TROPOMI	TROPOMI-LOTOS *a-priori*	32,3	56,7	0,83	-18,0	23,6	0,79

Lastly, it was possible to retrieve an emission dataset from actual TROPOMI observations that showed good agreement with the model-ingested emissions after replacing the TROPOMI TM5 *a-priori* with the high-resolution *a-priori* derived from LOTOS-EUROS. Emission hotspots were underestimated by -18%, while the overall domain showed an overestimation of 32%. This represents a good level of agreement, considering that the top-down satellite and bottom-up inventory emissions are fully independent pieces of information (observed versus reported emissions), and that the comparisons are done in a consistent way through the *a-priori* replacement.

The high-resolution model, incorporating prior knowledge of emission locations and strengths, provides important constraints on the spatial and temporal variability of NO_2 needed for quantitative comparisons. When bottom-up emissions significantly deviate from the real emissions, such as in cases of missing sources, this can result in errors in satellite-derived emissions of up to approximately 30%. These discrepancies can be reduced through iterative refinement, using satellite-derived emissions to update the model employed for generating the a *a-priori* estimates.

5 Conclusions

This study examined the FDA accuracy in reconstructing NO_x emissions by utilizing satellite-synthetic observations generated with a high-resolution 2x2 km^2 implementation of the LOTOS-EUROS CTM over the Netherlands. Overall, the FDA demonstrates good performance, achieving a satisfactory representation of the spatial variation of emissions, particularly from major emitters (R: 0,96), while maintaining relatively low levels of underestimation for emission hotspots (NMGE: -8,6% in the LOTOS-EUROS grid and -11,0% in the TROPOMI grid). However, this level of agreement is only achieved by using NO_2 VCD integrated up to PBL height, dynamically selecting wind fields, NO_2 lifetime, and NO_2 to NO_x conversion factors, all determined from the CTM output. This contrasts with the basic implementation of the method for actual satellite data, which in most cases relies on the total tropospheric column and fixed values for the aforementioned variables.

The sensitivity analyses provided the following insights. Using PBL NO_2 columns to drive the FDA results in a more accurate representation of emissions, reducing the generalized overestimation that occurs when using the tropospheric column. This improvement is because the entire tropospheric column includes NO_x from long-range transport and upper troposphere entrainment, which are not directly linked to the emissions being assessed during the FDA application. Additionally, chemical sinks within the PBL and the free troposphere operate differently.

Using 2D wind fields at different altitudes exhibited a minimal impact on the final emission estimate. This is potentially attributed to the flat terrain and relatively smooth wind patterns over the Netherlands and the consistency of these winds within a well-developed PBL, which is the case for the summer period and noon overpass times that were used in this study. In this study, ECMWF-IFS wind fields, with an original resolution of roughly 9 km, were downscaled to a high spatial resolution of about 2 x 2 km. Nonetheless, the FDA is often applied using coarser publicly available datasets, such as ERA5, with a horizontal resolution of 0,25 x 0,25 degrees. Such coarse datasets may not accurately capture the spatial variability of wind fields, especially in regions with complex topography, which can introduce artifacts in divergence estimation. In these scenarios, using higher-resolution wind fields is recommended.

On the contrary, incorporating the spatiotemporal variability of NO_x lifetimes and the conversion factors from NO_2 to NO_x using modeling data emerged as a crucial factor affecting the precision of NO_x emission derived from satellite data (Krol et al., 2024). The high-resolution model-derived lifetimes span a wide range of values, from as low as 2 hours in background conditions to over 20 hours over major sources, significantly diverging from the constant value of 4 hours proposed in the original FDA implementation. Employing model-derived lifetimes and NO_2 to NO_x conversion factors reduced the NMB for both hotspots and background regions.

The long lifetimes at the hotspots and within the pollution plumes imply that the sink term is small. Therefore, estimated emissions at the source are mainly dependent on the divergence and can be computed accurately regardless of the uncertainty of the lifetime estimations, as long as the numerical smearing effect can be compensated. The opposite however applies when deriving emissions in the background regions where the sink term is significant owing to the shorter lifetimes. Indeed, for deriving total emissions at the simulation domain and at country level, in the cases where there is no significant inflow or outflow of NO_x through the boundaries, the emissions are directly proportional to the sink term and depend crucially on the lifetime estimate.

When handling real TROPOMI data, substituting the default TM5-MP a *a-priori* with a more refined version derived from advanced high-resolution CTM simulations will mitigate the underestimation of hotspot emissions. This study revealed that emissions estimated with the TROPOMI LOTOS-EUROS *a-priori* product were 34% higher over the hotspots compared to the default TM5-MP *a-priori*.

Lastly, the runs conducted to test the FDA applicability outside the usual TROPOMI overpass time exhibit extensive areas with negative emission artifacts for the 08:00 LT test, and a generalized emission overestimation for the 18:00 LT test. These errors stem from ignoring the accumulation or depletion of atmospheric NO_x during non-stable conditions, thereby invalidating the steady-state assumption of the FDA, and by remaining biases in the lifetime estimates. These findings suggest that the application of the FDA method to observations from geostationary sensors, such as TEMPO, GEMS, and the forthcoming

Sentinel-4 sensor, is more complex than applications during noontime observations, such as those from TROPOMI. In such cases, it is necessary to disregard the steady-state assumption and include the dV/dt term to account for the buildup or depletion of atmospheric $\mathrm{NO_x}$. Furthermore, losses due to deposition and chemical reactions beyond the formation of $\mathrm{HNO_3}$, such as oxidation leading to the production of alkyl and multifunctional nitrates, may play a more significant role, hence the assumptions underlying the $\mathrm{NO_2}$ lifetime estimates might not be valid.

Code and data availability. The code V1.0 used in this paper to perform the end-to-end test of the flux divergence approach is accessible on Zenodo (https://doi.org/10.5281/zenodo.13268654, Cifuentes et al., 2024), along with a sample of the LOTOS-EUROS modeling outputs required to run the code. The complete set of modeling outputs can be provided upon request. The TROPOMI L2 NO2 datasets used in this study are publicly available through the Copernicus Data Space Ecosystem (https://dataspace.copernicus.eu, last accessed: 08 August 2024).

Appendix A: Statistical performance metrics

$$NMB = \frac{\sum_{i=1}^{n} P_i - O_i}{\sum_{i=1}^{n} O_i} \tag{A1}$$

$$NMGE = \frac{\sum_{i=1}^{n} |P_i - O_i|}{\sum_{i=1}^{n} O_i} \tag{A2}$$

Where n represents the total number of pixels, P is the predicted emissions at a given pixel i, and O is the original emissions ingested in the CTMs for pixel i.

Appendix B: Supporting figures

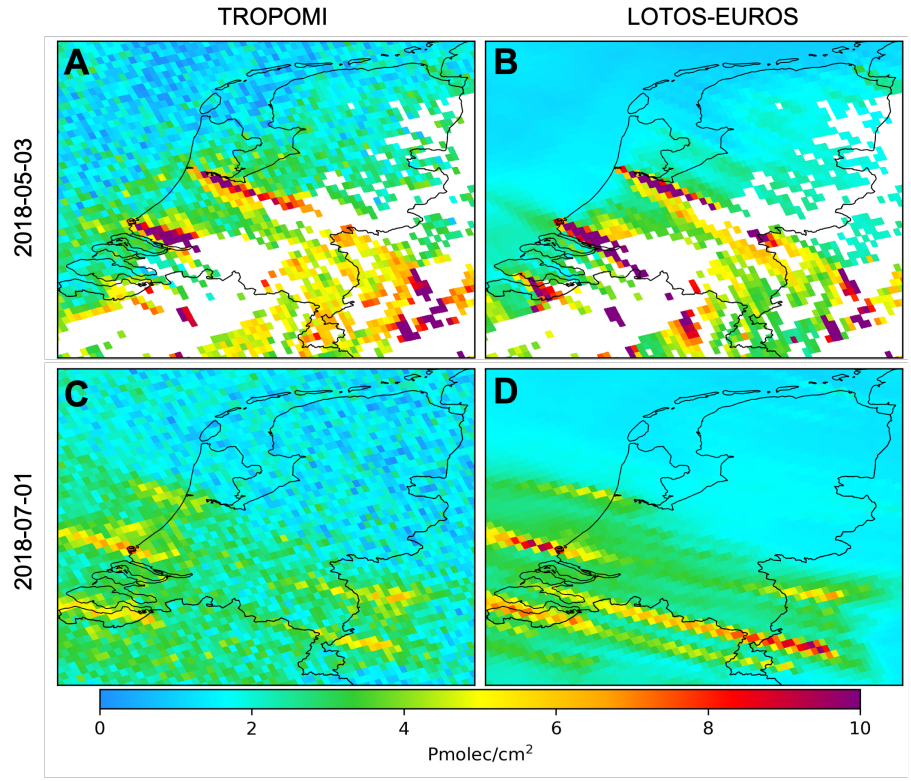

Figure A1. Daily NO_2 tropospheric vertical column densities over the Netherlands, as observed by TROPOMI and simulated using LOTOS-EUROS. **(A)** TROPOMI NO_2 VCD for May 3, 2018. **(B)** LOTOS-EUROS NO_2 VCD for May 3, 2018. **(C)** TROPOMI NO_2 VCD for July 1, 2018. **(D)** LOTOS-EUROS NO_2 VCD for July 1, 2018.

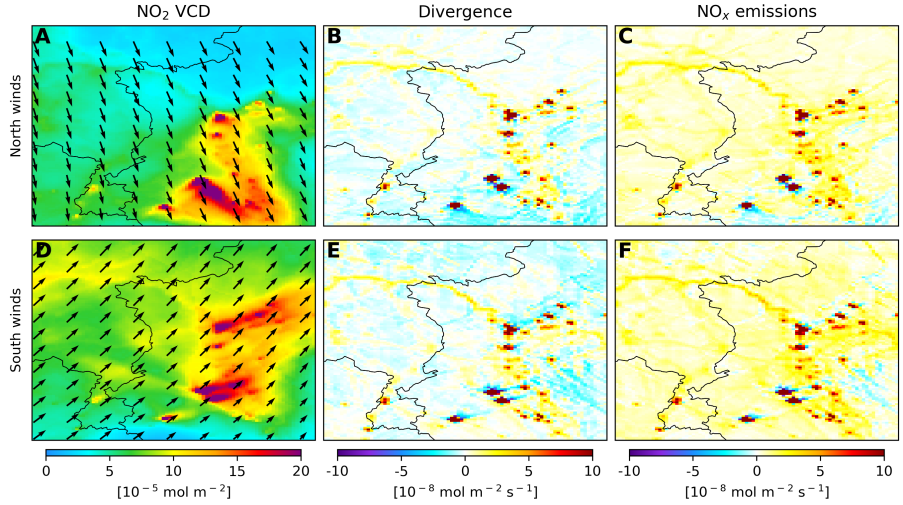

Figure A2. Mean NO_x emissions and flux divergence derived from the synthetic dataset at LOTOS-EUROS native resolution using configuration ID07, aggregated by predominantly southerly and northerly winds. **(A)** Mean NO_2 vertical column density for days with predominantly north winds. **(B)** Mean NO_x flux divergence for days with predominantly north winds. **(C)** Mean NO_x emissions for days with predominantly north winds. **(D)** Mean NO_2 vertical column density for days with predominantly south winds. **(E)** Mean NO_x flux divergence for days with predominantly south winds. **(F)** Mean NO_x emissions for days with predominantly south winds.

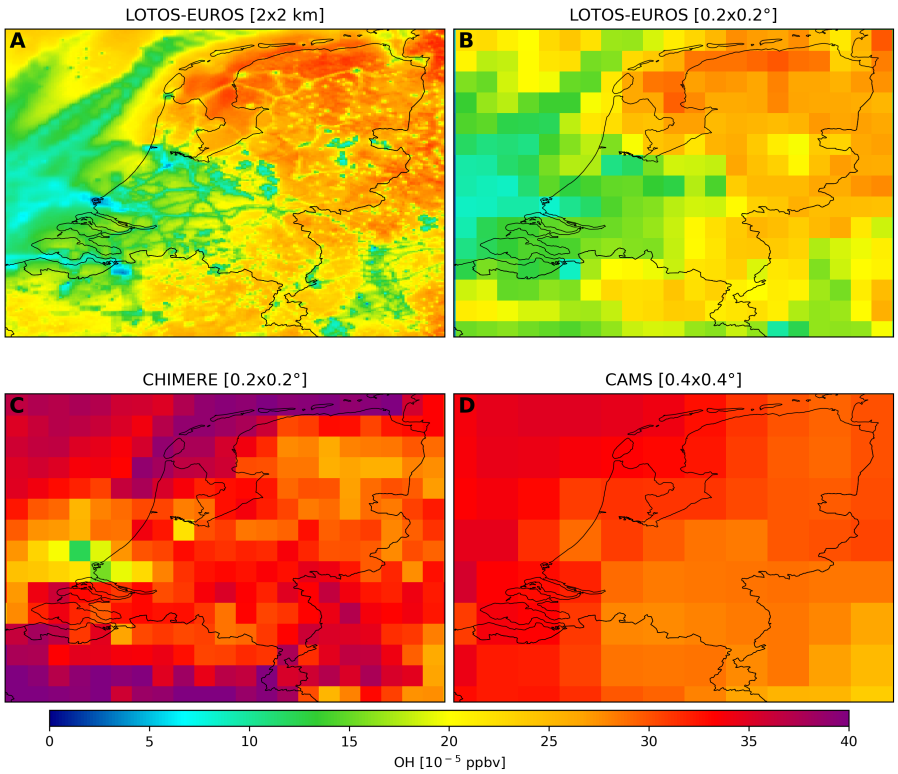

Figure A3. Mean ground OH concentration for JJA 2018 at 12:00 LT. **(A)** LOTOS-EUROS run at 2x2 km. **(B)** LOTOS-EUROS run at 0.2x0.2°. **(C)** Chimere run at 0.2x0.2°. **(D)** CAMS forecast at 0.4x0.4°.

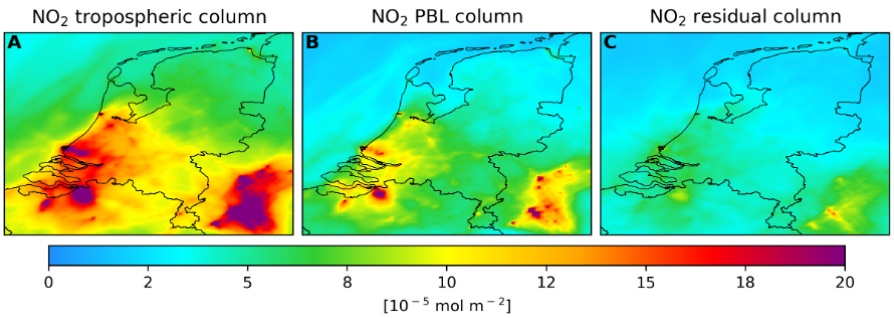

Figure A4. Mean NO_2 columns integrated up to the tropopause **(A)** and within the PBL **(B)**, and residual column **(c)** over the Netherlands for June, July, and August at the typical TROPOMI overpass time.

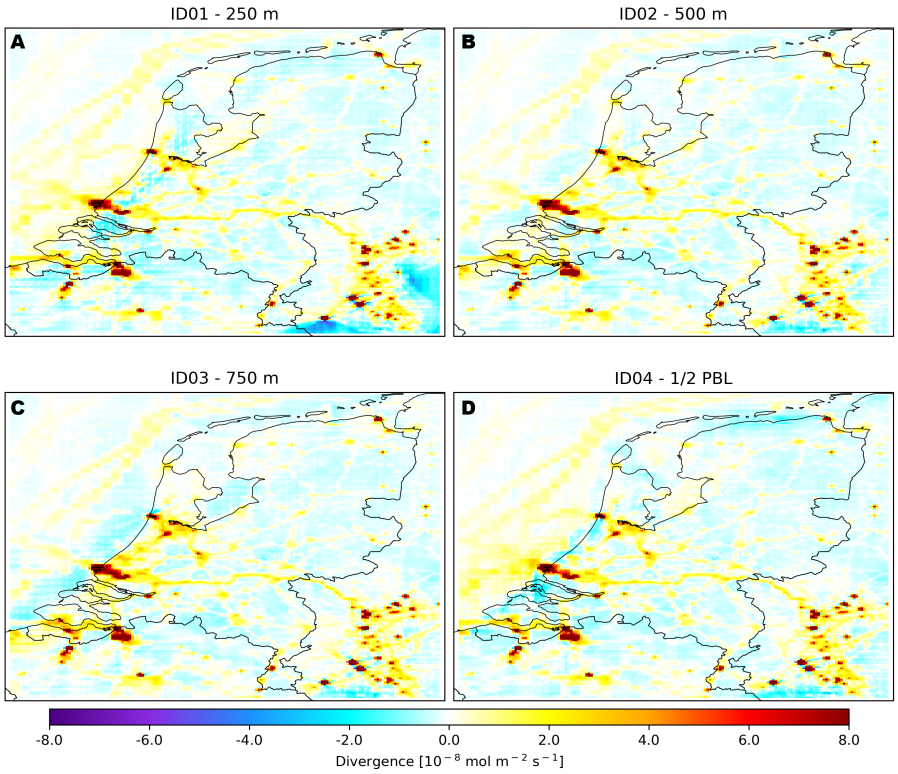

Figure A5. Mean NO_x flux divergence for June, July, and August (JJA) using different altitudes for the wind fields. **(A)** 250 m. **(B)** 500 m. **(C)** 750 m. **(D)** Winds extracted at half planetary boundary layer height altitude

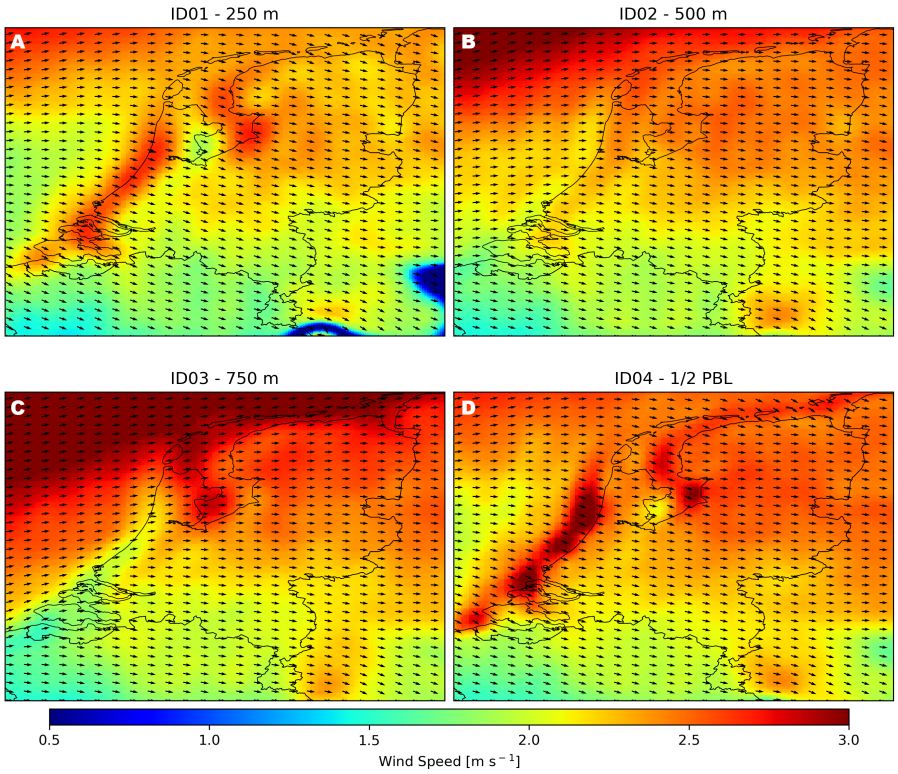

Figure A6. Mean wind fields for June, July, and August (JJA) at different altitudes. **(A)** 250 m. **(A)** 500 m. **(A)** 750 m. **(A)** Winds extracted at half planetary boundary layer height altitude.

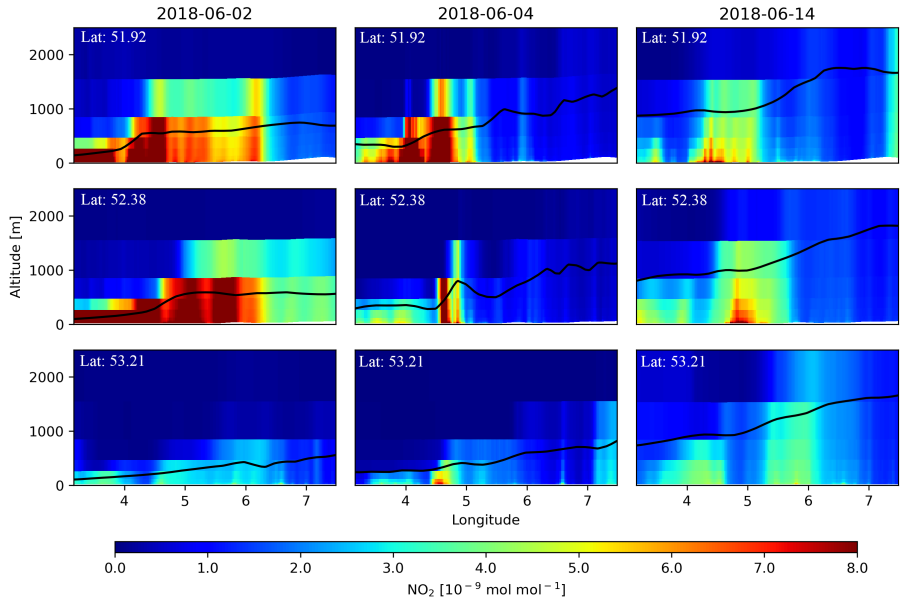

Figure A7. Latitudinal cross-sections of planetary boundary layer height and NO_2 concentrations at 13:30 LT extracted from LOTOS-EUROS simulation.

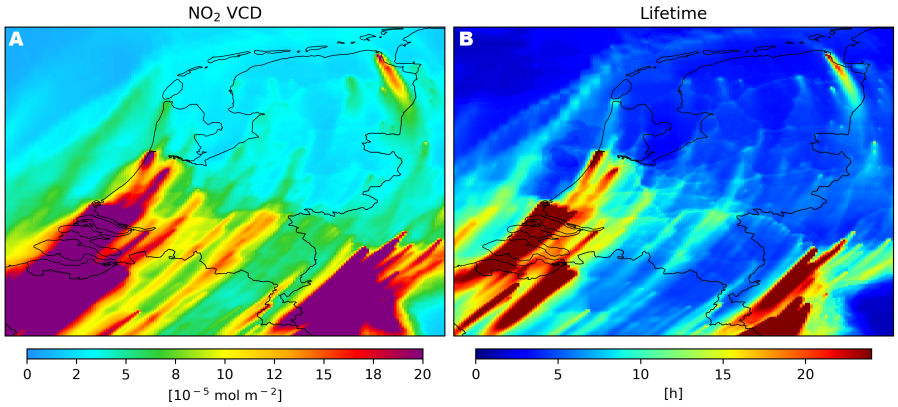

Figure A8. Example of NO_2 lifetime on a daily basis at satellite overpass time. **(A)** NO_2 vertical column density for a given day at satellite overpass time. **(B)** NO_2-weigthed lifetime derived from LOTOS-EUROS OH and T.

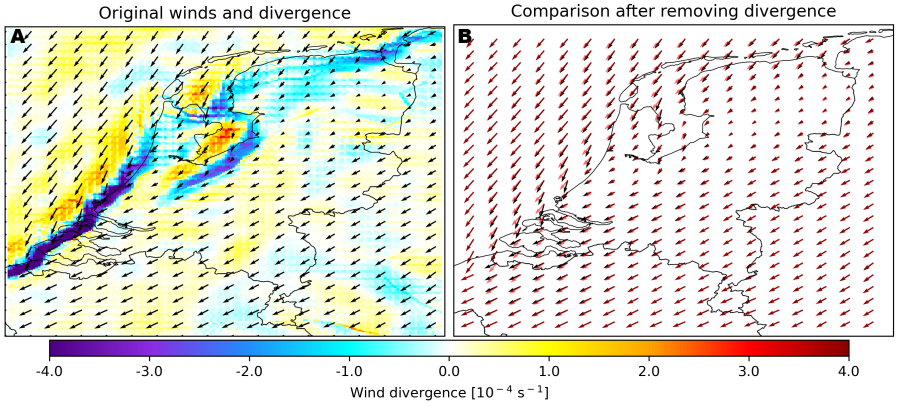

Figure A9. Example of ECMWF-IFS wind fields before and after reducing the divergence of the wind. **(A)** Original wind fields and corresponding wind divergence for a given day. **(B)** Original wind fields (black) and divergence-free wind fields obtained using the iterative algorithm proposed by Bryan (2022) (red).

Author contributions. **Felipe Cifuentes:** Methodology, Software, Formal analysis, Writing - Original Draft, Visualization. **Henk Eskes:** Conceptualization, Validation, Writing - Review and Editing, Supervision, Project administration, Funding acquisition. **Folkert Boersma:** Conceptualization, Validation, Writing - Review and Editing, Supervision. **Enrico Dammers:** Methodology, Writing - Review and Editing. **Charlotte Bryan:** Conceptualization, Software.

Competing interests. The authors declare that they have no known competing financial or personal interests that could have influenced the work reported in this paper.

Acknowledgements. This study was funded by the Dutch Ministry of Agriculture, Nature and Food Quality (LNV), within the framework of the National Nitrogen Knowledge Programme (NKS), project NKS-SAGEN on satellite observations and ensemble modeling.

References

Allen, D., Pickering, K. E., Bucsela, E., Geffen, J. V., Lapierre, J., Koshak, W., and Eskes, H.: Observations of Lightning NOx Production From Tropospheric Monitoring Instrument Case Studies Over the United States, Journal of Geophysical Research: Atmospheres, 126, https://doi.org/10.1029/2020JD034174, 2021.

Beirle, S., Platt, U., Wenig, M., and Wagner, T.: Weekly cycle of NO_2 by GOME measurements: a signature of anthropogenic sources, Atmospheric Chemistry and Physics, 3, 2225–2232, https://doi.org/10.5194/acp-3-2225-2003, 2003.

Beirle, S., Boersma, K. F., Platt, U., Lawrence, M. G., and Wagner, T.: Megacity Emissions and Lifetimes of Nitrogen Oxides Probed from Space, Science, 333, 1737–1739, https://doi.org/10.1126/science.1207824, 2011.

Beirle, S., Borger, C., Dörner, S., Li, A., Hu, Z., Liu, F., Wang, Y., and Wagner, T.: Pinpointing nitrogen oxide emissions from space, Science Advances, 5, https://doi.org/10.1126/SCIADV.AAX9800, 2019.

Beirle, S., Borger, C., Dörner, S., Eskes, H., Kumar, V., Laat, A. D., and Wagner, T.: Catalog of NOx emissions from point sources as derived from the divergence of the NO2 flux for TROPOMI, Earth System Science Data, 13, 2995–3012, https://doi.org/10.5194/ESSD-13-2995-2021, 2021.

Beirle, S., Borger, C., Jost, A., and Wagner, T.: Improved catalog of NO_x point source emissions (version 2), Earth System Science Data, 15, 3051–3073, https://doi.org/10.5194/essd-15-3051-2023, 2023.

Bessagnet, B., Pirovano, G., Mircea, M., Cuvelier, C., Aulinger, A., Calori, G., Ciarelli, G., Manders, A., Stern, R., Tsyro, S., García Vivanco, M., Thunis, P., Pay, M.-T., Colette, A., Couvidat, F., Meleux, F., Rouïl, L., Ung, A., Aksoyoglu, S., Baldasano, J. M., Bieser, J., Briganti, G., Cappelletti, A., D'Isidoro, M., Finardi, S., Kranenburg, R., Silibello, C., Carnevale, C., Aas, W., Dupont, J.-C., Fagerli, H., Gonzalez, L., Menut, L., Prévôt, A. S. H., Roberts, P., and White, L.: Presentation of the EURODELTA III intercomparison exercise – evaluation of the chemistry transport models' performance on criteria pollutants and joint analysis with meteorology, Atmospheric Chemistry and Physics, 16, 12 667–12 701, https://doi.org/10.5194/acp-16-12667-2016, 2016.

Boersma, K. F., Jacob, D. J., Trainic, M., Rudich, Y., DeSmedt, I., Dirksen, R., and Eskes, H. J.: Validation of urban NO_2 concentrations and their diurnal and seasonal variations observed from the SCIAMACHY and OMI sensors using in situ surface measurements in Israeli cities, Atmospheric Chemistry and Physics, 9, 3867–3879, https://doi.org/10.5194/acp-9-3867-2009, 2009.

Bryan, C.: The Flux Divergence Method Applied to Nitrogen Emissions in The Netherlands, available at http://resolver.tudelft.nl/uuid:6e7e611b-9a7a-4886-8eb8-f1a172516d99, 2022.

Chan, K. L., Wiegner, M., van Geffen, J., De Smedt, I., Alberti, C., Cheng, Z., Ye, S., and Wenig, M.: MAX-DOAS measurements of tropospheric NO₂ and HCHO in Munich and the comparison to OMI and TROPOMI satellite observations, Atmospheric Measurement Techniques, 13, 4499–4520, https://doi.org/10.5194/amt-13-4499-2020, 2020.

Chen, Y., van der A, R. J., Ding, J., Eskes, H., Williams, J. E., Theys, N., Tsikerdekis, A., and Levelt, P. F.: SO_2 emissions and lifetimes derived from TROPOMI observations over India using a flux-divergence method, EGUsphere, 2024, 1–26, https://doi.org/10.5194/egusphere-2024-1094, 2024.

Chen, Y. C., Chou, C. C., Liu, C. Y., Chi, S. Y., and Chuang, M. T.: Evaluation of the nitrogen oxide emission inventory with TROPOMI observations, Atmospheric Environment, 298, 119 639, https://doi.org/10.1016/J.ATMOSENV.2023.119639, 2023.

Clark, C. M., Bai, Y., Bowman, W. D., Cowles, J. M., Fenn, M. E., Gilliam, F. S., Phoenix, G. K., Siddique, I., Stevens, C. J., Sverdrup, H. U., and Throop, H. L.: Nitrogen Deposition and Terrestrial Biodiversity, Encyclopedia of Biodiversity: Second Edition, pp. 519–536, https://doi.org/10.1016/B978-0-12-384719-5.00366-X, 2013.

Colette, A., Andersson, C., Manders, A., Mar, K., Mircea, M., Pay, M.-T., Raffort, V., Tsyro, S., Cuvelier, C., Adani, M., Bessagnet, B., Bergström, R., Briganti, G., Butler, T., Cappelletti, A., Couvidat, F., D'Isidoro, M., Doumbia, T., Fagerli, H., Granier, C., Heyes, C., Klimont, Z., Ojha, N., Otero, N., Schaap, M., Sindelarova, K., Stegehuis, A. I., Roustan, Y., Vautard, R., van Meijgaard, E., Vivanco, M. G., and Wind, P.: EURODELTA-Trends, a multi-model experiment of air quality hindcast in Europe over 1990–2010, Geoscientific Model Development, 10, 3255–3276, https://doi.org/10.5194/gmd-10-3255-2017, 2017.

Cooper, M., Martin, R. V., Padmanabhan, A., and Henze, D. K.: Comparing mass balance and adjoint methods for inverse modeling of nitrogen dioxide columns for global nitrogen oxide emissions, Journal of Geophysical Research: Atmospheres, 122, 4718–4734, https://doi.org/https://doi.org/10.1002/2016JD025985, 2017.

Dammers, E., Tokaya, J., Mielke, C., Hausmann, K., Griffin, D., McLinden, C., Eskes, H., and Timmermans, R.: Can TROPOMI-NO_2 satellite data be used to track the drop and resurgence of NO_x emissions between 2019–2021 using the multi-source plume method (MSPM)?, Geoscientific Model Development Discussions, 2022, 1–33, https://doi.org/10.5194/gmd-2022-292, 2022.

Dammers, E., Tokaya, J., Mielke, C., Hausmann, K., Griffin, D., McLinden, C., Eskes, H., and Timmermans, R.: Can TROPOMI NO_2 satellite data be used to track the drop in and resurgence of NO_x emissions in Germany between 2019–2021 using the multi-source plume method (MSPM)?, Geoscientific Model Development, 17, 4983–5007, https://doi.org/10.5194/gmd-17-4983-2024, 2024.

de Foy, B., Schauer, J. J., Lorente, A., al, Tian, Y., Sun, Y., Borsdorff, T., Wu, N., Geng, G., and Yan, L.: An improved understanding of NOx emissions in South Asian megacities using TROPOMI NO2 retrievals, Environmental Research Letters, 17, 024 006, https://doi.org/10.1088/1748-9326/AC48B4, 2022.

de Vries, W.: Impacts of nitrogen emissions on ecosystems and human health: A mini review, Current Opinion in Environmental Science Health, 21, 100 249, https://doi.org/10.1016/J.COESH.2021.100249, 2021.

Ding, J., van der A, R. J., Mijling, B., and Levelt, P. F.: Space-based NO_x emission estimates over remote regions improved in DECSO, Atmospheric Measurement Techniques, 10, 925–938, https://doi.org/10.5194/amt-10-925-2017, 2017.

Dix, B., Francoeur, C., Li, M., Serrano-Calvo, R., Levelt, P., Veefkind, J., McDonald, B., and De Gouw, J.: Quantifying NOx-Emissions from U.S. Oil and Gas Production Regions Using TROPOMI NO2, ACS Earth and Space Chemistry, 6, 403–414, https://doi.org/10.1021/acsearthspacechem.1c00387, 2022.

Douros, J., Eskes, H., van Geffen, J., Boersma, K. F., Compernolle, S., Pinardi, G., Blechschmidt, A.-M., Peuch, V.-H., Colette, A., and Veefkind, P.: Comparing Sentinel-5P TROPOMI NO_2 column observations with the CAMS regional air quality ensemble, Geoscientific Model Development, 16, 509–534, https://doi.org/10.5194/gmd-16-509-2023, 2023.

Eastham, S. D. and Jacob, D. J.: Limits on the ability of global Eulerian models to resolve intercontinental transport of chemical plumes, Atmospheric Chemistry and Physics, 17, 2543–2553, https://doi.org/10.5194/acp-17-2543-2017, 2017.

Eskes, H., van Geffen, J., Boersma, K. F., Eichmann, K.-U., Apituley, A., Pedergnana, M., Sneep, M., Veefkind, P., and Loyola, D.: Sentinel-5 precursor/TROPOMI Level 2 Product User Manual Nitrogendioxide. S5P-KNMI-L2-0021-MA, 2022.

Fioletov, V., McLinden, C. A., Griffin, D., Theys, N., Loyola, D. G., Hedelt, P., Krotkov, N. A., and Li, C.: Anthropogenic and volcanic point source SO_2 emissions derived from TROPOMI on board Sentinel-5 Precursor: first results, Atmospheric Chemistry and Physics, 20, 5591–5607, https://doi.org/10.5194/acp-20-5591-2020, 2020.

Fioletov, V., McLinden, C. A., Griffin, D., Krotkov, N., Liu, F., and Eskes, H.: Quantifying urban, industrial, and background changes in NO_2 during the COVID-19 lockdown period based on TROPOMI satellite observations, Atmospheric Chemistry and Physics, 22, 4201–4236, https://doi.org/10.5194/acp-22-4201-2022, 2022.

Georgoulias, A. K., Boersma, K. F., Vliet, J. V., Zhang, X., A, R. V. D., Zanis, P., and Laat, J. D.: Detection of NO2 pollution plumes from individual ships with the TROPOMI/S5P satellite sensor, Environmental Research Letters, 15, https://doi.org/10.1088/1748-9326/ABC445, 2020.

Goldberg, D. L., Lu, Z., Streets, D. G., Foy, B. D., Griffin, D., Mclinden, C. A., Lamsal, L. N., Krotkov, N. A., and Eskes, H.: Enhanced Capabilities of TROPOMI NO2: Estimating NOX from North American Cities and Power Plants, Environmental Science and Technology, 53, 12 594–12 601, https://doi.org/10.1021/ACS.EST.9B04488, 2019.

Goldberg, D. L., Harkey, M., Foy, B. D., Judd, L., Johnson, J., Yarwood, G., and Holloway, T.: Evaluating NOx emissions and their effect on O3 production in Texas using TROPOMI NO2 and HCHO, Atmos. Chem. Phys, 22, https://doi.org/10.5194/acp-22-10875-2022, 2022.

Griffin, D., Zhao, X., Mclinden, C., Boersma, K., Bourassa, A., Dammers, E., Degenstein, D., Eskes, H., Fehr, L., Fioletov, V., Hayden, K., Kharol, S., Li, S., Makar, P., Martin, R., Mihele, C., Mittermeier, R., Krotkov, N., Sneep, M., and Wolde, M.: High-Resolution Mapping of Nitrogen Dioxide With TROPOMI: First Results and Validation Over the Canadian Oil Sands, Geophysical Research Letters, 46, https://doi.org/10.1029/2018GL081095, 2019.

Griffin, D., McLinden, C. A., Dammers, E., Adams, C., Stockwell, C. E., Warneke, C., Bourgeois, I., Peischl, J., Ryerson, T. B., Zarzana, K. J., Rowe, J. P., Volkamer, R., Knote, C., Kille, N., Koenig, T. K., Lee, C. F., Rollins, D., Rickly, P. S., Chen, J., Fehr, L., Bourassa, A., Degenstein, D., Hayden, K., Mihele, C., Wren, S. N., Liggio, J., Akingunola, A., and Makar, P.: Biomass burning nitrogen dioxide emissions derived from space with TROPOMI: methodology and validation, Atmospheric Measurement Techniques, 14, 7929–7957, https://doi.org/10.5194/amt-14-7929-2021, 2021.

Hakkarainen, J., Ialongo, I., Koene, E., Szeląg, M. E., Tamminen, J., Kuhlmann, G., and Brunner, D.: Analyzing Local Carbon Dioxide and Nitrogen Oxide Emissions From Space Using the Divergence Method: An Application to the Synthetic SMARTCARB Dataset, Frontiers in Remote Sensing, 3, https://doi.org/10.3389/frsen.2022.878731, 2022.

Hakkarainen, J., Kuhlmann, G., Koene, E., Santaren, D., Meier, S., Krol, M. C., van Stratum, B. J., Ialongo, I., Chevallier, F., Tamminen, J., Brunner, D., and Broquet, G.: Analyzing nitrogen dioxide to nitrogen oxide scaling factors for data-driven satellite-based emission estimation methods: A case study of Matimba/Medupi power stations in South Africa, Atmospheric Pollution Research, 15, 102 171, https://doi.org/https://doi.org/10.1016/j.apr.2024.102171, 2024.

Huber, D. E., Steiner, A. L., and Kort, E. A.: Daily Cropland Soil NOx Emissions Identified by TROPOMI and SMAP, Geophysical Research Letters, 47, https://doi.org/10.1029/2020GL089949, 2020.

Ialongo, I., Virta, H., Eskes, H., Hovila, J., and Douros, J.: Comparison of TROPOMI/Sentinel-5 Precursor NO₂ observations with ground-based measurements in Helsinki, Atmospheric Measurement Techniques, 13, 205–218, https://doi.org/10.5194/amt-13-205-2020, 2020.

Judd, L. M., Al-Saadi, J. A., Szykman, J. J., Valin, L. C., Janz, S. J., Kowalewski, M. G., Eskes, H. J., Veefkind, J. P., Cede, A., Mueller, M., Gebetsberger, M., Swap, R., Pierce, R. B., Nowlan, C. R., Abad, G. G., Nehrir, A., and Williams, D.: Evaluating Sentinel-5P TROPOMI tropospheric NO_2 column densities with airborne and Pandora spectrometers near New York City and Long Island Sound, Atmospheric Measurement Techniques, 13, 6113–6140, https://doi.org/10.5194/amt-13-6113-2020, 2020.

Koene, E. F. M., Brunner, D., and Kuhlmann, G.: On the Theory of the Divergence Method for Quantifying Source Emissions From Satellite Observations, Journal of Geophysical Research: Atmospheres, 129, e2023JD039 904, https://doi.org/https://doi.org/10.1029/2023JD039904, 2024.

Krol, M., van Stratum, B., Anglou, I., and Boersma, K. F.: Estimating NO_x emissions of stack plumes using a high-resolution atmospheric chemistry model and satellite-derived NO_2 columns, EGUsphere, 2024, 1–32, https://doi.org/10.5194/egusphere-2023-2519, 2024.

Kurchaba, S., van Vliet, J., Verbeek, F. J., Meulman, J. J., and Veenman, C. J.: Supervised Segmentation of NO2 Plumes from Individual Ships Using TROPOMI Satellite Data, Remote Sensing, 14, https://doi.org/10.3390/RS14225809, 2022.

Lambert, J.-C., Keppens, A., Compernolle, S., Eichmann, K.-U., de Graaf, M., Hubert, D., Langerock, B., Ludewig, A., Sha, M., Verhoelst, T., Wagner, T., Ahn, C., Argyrouli, A., Balis, D., Chan, K., Coldewey-Egbers, M., Smedt, I. D., Eskes, H., Fjæraa, A., Garane, K., Gleason, J., Goutail, F., Granville, J., Hedelt, P., Ahn, C., Heue, K.-P., Jaross, G., Kleipool, Q., Koukouli, M., Lutz, R., Velarte, M. M., Michailidis, K., Nanda, S., Niemeijer, S., Pazmiño, A., Pinardi, G., Richter, A., Rozemeijer, N., Sneep, M., Zweers, D. S., Theys, N., Tilstra, G., Torres, O., Valks, P., van Geffen, J., Vigouroux, C., Wang, P., and Weber, M.: A Quarterly Validation Report of the Copernicus Sentinel-5 Precursor Operational Data Products 21: April 2018 – November 2023., S5P MPC Routine Operations Consolidated Validation Report series, p. 194, 2023.

Lange, K., Richter, A., and Burrows, J. P.: Variability of nitrogen oxide emission fluxes and lifetimes estimated from Sentinel-5P TROPOMI observations, Atmospheric Chemistry and Physics, 22, 2745–2767, https://doi.org/10.5194/acp-22-2745-2022, 2022.

Laughner, J. L. and Cohen, R. C.: Direct observation of changing NOx lifetime in North American cities, Science, 366, 723–727, https://doi.org/10.1126/science.aax6832, 2019.

Laughner, J. L., Zare, A., and Cohen, R. C.: Effects of daily meteorology on the interpretation of space-based remote sensing of NO_2, Atmospheric Chemistry and Physics, 16, 15 247–15 264, https://doi.org/10.5194/acp-16-15247-2016, 2016.

Leguijt, G., Maasakkers, J. D., Denier van der Gon, H. A. C., Segers, A. J., Borsdorff, T., and Aben, I.: Quantification of carbon monoxide emissions from African cities using TROPOMI, Atmospheric Chemistry and Physics, 23, 8899–8919, https://doi.org/10.5194/acp-23-8899-2023, 2023.

Li, C., Martin, R. V., Cohen, R. C., Bindle, L., Zhang, D., Chatterjee, D., Weng, H., and Lin, J.: Variable effects of spatial resolution on modeling of nitrogen oxides, Atmospheric Chemistry and Physics, 23, 3031–3049, https://doi.org/10.5194/acp-23-3031-2023, 2023.

Li, J., Wang, Y., Zhang, R., Smeltzer, C., Weinheimer, A., Herman, J., Boersma, K. F., Celarier, E. A., Long, R. W., Szykman, J. J., Delgado, R., Thompson, A. M., Knepp, T. N., Lamsal, L. N., Janz, S. J., Kowalewski, M. G., Liu, X., and Nowlan, C. R.: Comprehensive evaluations of diurnal NO_2 measurements during DISCOVER-AQ 2011: effects of resolution-dependent representation of NO_x emissions, Atmospheric Chemistry and Physics, 21, 11 133–11 160, https://doi.org/10.5194/acp-21-11133-2021, 2021.

Lin, X., van der A, R., de Laat, J., Huijnen, V., Mijling, B., Ding, J., Eskes, H., Douros, J., Liu, M., Zhang, X., and Liu, Z.: European soil NOx emissions derived from satellite NO2 observations, ESS Open Archive, pre-print, 2023.

Liu, F., Tao, Z., Beirle, S., Joiner, J., Yoshida, Y., Smith, S. J., Knowland, K. E., and Wagner, T.: A new method for inferring city emissions and lifetimes of nitrogen oxides from high-resolution nitrogen dioxide observations: A model study, Atmospheric Chemistry and Physics, 22, 1333–1349, https://doi.org/10.5194/ACP-22-1333-2022, 2022.

Liu, M., Lin, J., Kong, H., Boersma, K. F., Eskes, H., Kanaya, Y., He, Q., Tian, X., Qin, K., Xie, P., Spurr, R., Ni, R., Yan, Y., Weng, H., and Wang, J.: A new TROPOMI product for tropospheric NO_2 columns over East Asia with explicit aerosol corrections, Atmospheric Measurement Techniques, 13, 4247–4259, https://doi.org/10.5194/amt-13-4247-2020, 2020.

Liu, M., van der A, R., van Weele, M., Eskes, H., Lu, X., Veefkind, P., de Laat, J., Kong, H., Wang, J., Sun, J., Ding, J., Zhao, Y., and Weng, H.: A New Divergence Method to Quantify Methane Emissions Using Observations of Sentinel-5P TROPOMI, Geophysical Research Letters, 48, https://doi.org/10.1029/2021GL094151, 2021.

Lonsdale, C. R. and Sun, K.: Nitrogen oxides emissions from selected cities in North America, Europe, and East Asia observed by the TROPOspheric Monitoring Instrument (TROPOMI) before and after the COVID-19 pandemic, Atmos. Chem. Phys, 23, 8727–8748, https://doi.org/10.5194/acp-23-8727-2023, 2023.

Lorente, A., Boersma, K. F., Eskes, H. J., Veefkind, J. P., van Geffen, J. H., de Zeeuw, M. B., van der Gon, H. A. D., Beirle, S., and Krol, M. C.: Quantification of nitrogen oxides emissions from build-up of pollution over Paris with TROPOMI, Scientific Reports, 9, https://doi.org/10.1038/S41598-019-56428-5, 2019.

Lu, X., Jacob, D. J., Wang, H., Maasakkers, J. D., Zhang, Y., Scarpelli, T. R., Shen, L., Qu, Z., Sulprizio, M. P., Nesser, H., Bloom, A. A., Ma, S., Worden, J. R., Fan, S., Parker, R. J., Boesch, H., Gautam, R., Gordon, D., Moran, M. D., Reuland, F., Villasana, C. A. O., and Andrews, A.: Methane emissions in the United States, Canada, and Mexico: evaluation of national methane emission inventories and 2010–2017 sectoral trends by inverse analysis of in situ (GLOBALVIEWplus CH_4 ObsPack) and satellite (GOSAT) atmospheric observations, Atmospheric Chemistry and Physics, 22, 395–418, https://doi.org/10.5194/acp-22-395-2022, 2022.

Manders, A. M. M., Builtjes, P. J. H., Curier, L., Denier van der Gon, H. A. C., Hendriks, C., Jonkers, S., Kranenburg, R., Kuenen, J. J. P., Segers, A. J., Timmermans, R. M. A., Visschedijk, A. J. H., Wichink Kruit, R. J., van Pul, W. A. J., Sauter, F. J., van der Swaluw, E., Swart, D. P. J., Douros, J., Eskes, H., van Meijgaard, E., van Ulft, B., van Velthoven, P., Banzhaf, S., Mues, A. C., Stern, R., Fu, G., Lu, S., Heemink, A., van Velzen, N., and Schaap, M.: Curriculum vitae of the LOTOS–EUROS (v2.0) chemistry transport model, Geoscientific Model Development, 10, 4145–4173, https://doi.org/10.5194/gmd-10-4145-2017, 2017.

Manders, A. M. M., Segers, A. J., and Jonkers, S.: LOTOS-EUROS v2.2.002 Reference Guide, https://airqualitymodeling.tno.nl/publish/pages/3175/lotos-euros-reference-guide.pdf, 2021.

Misra, P., Takigawa, M., Khatri, P., Dhaka, S. K., Dimri, A. P., Yamaji, K., Kajino, M., Takeuchi, W., Imasu, R., Nitta, K., Patra, P. K., and Hayashida, S.: Nitrogen oxides concentration and emission change detection during COVID-19 restrictions in North India, Scientific Reports 2021 11:1, 11, 1–11, https://doi.org/10.1038/s41598-021-87673-2, 2021.

Murray, L. T.: Lightning NO x and Impacts on Air Quality, Current Pollution Reports 2016 2:2, 2, 115–133, https://doi.org/10.1007/S40726-016-0031-7, 2016.

Nicely, J. M., Salawitch, R. J., Canty, T., Anderson, D. C., Arnold, S. R., Chipperfield, M. P., Emmons, L. K., Flemming, J., Huijnen, V., Kinnison, D. E., Lamarque, J.-F., Mao, J., Monks, S. A., Steenrod, S. D., Tilmes, S., and Turquety, S.: Quantifying the causes of differences in tropospheric OH within global models, Journal of Geophysical Research: Atmospheres, 122, 1983–2007, https://doi.org/https://doi.org/10.1002/2016JD026239, 2017.

Nicely, J. M., Duncan, B. N., Hanisco, T. F., Wolfe, G. M., Salawitch, R. J., Deushi, M., Haslerud, A. S., Jöckel, P., Josse, B., Kinnison, D. E., Klekociuk, A., Manyin, M. E., Marécal, V., Morgenstern, O., Murray, L. T., Myhre, G., Oman, L. D., Pitari, G., Pozzer, A., Quaglia, I., Revell, L. E., Rozanov, E., Stenke, A., Stone, K., Strahan, S., Tilmes, S., Tost, H., Westervelt, D. M., and Zeng, G.: A machine learning examination of hydroxyl radical differences among model simulations for CCMI-1, Atmospheric Chemistry and Physics, 20, 1341–1361, https://doi.org/10.5194/acp-20-1341-2020, 2020.

Penn, E. and Holloway, T.: Evaluating current satellite capability to observe diurnal change in nitrogen oxides in preparation for geostationary satellite missions, Environmental Research Letters, 15, 034 038, https://doi.org/10.1088/1748-9326/ab6b36, 2020.

Petersen, A. K., Brasseur, G. P., Bouarar, I., Flemming, J., Gauss, M., Jiang, F., Kouznetsov, R., Kranenburg, R., Mijling, B., Peuch, V.-H., Pommier, M., Segers, A., Sofiev, M., Timmermans, R., van der A, R., Walters, S., Xie, Y., Xu, J., and Zhou, G.: Ensemble forecasts of air quality in eastern China – Part 2: Evaluation of the MarcoPolo–Panda prediction system, version 1, Geoscientific Model Development, 12, 1241–1266, https://doi.org/10.5194/gmd-12-1241-2019, 2019.

Peuch, V.-H., Engelen, R., Rixen, M., Dee, D., Flemming, J., Suttie, M., Ades, M., Agusti-Panareda, A., Ananasso, C., Andersson, E., Armstrong, D., BarrÃ©, J., Bousserez, N., Dominguez, J., Garrigues, S., Inness, A., Jones, L., Kipling, Z., Letertre-Danczak, J., and ThÃ©paut,

J.-N.: The Copernicus Atmosphere Monitoring Service: From Research to Operations, Bulletin of the American Meteorological Society, 103, https://doi.org/10.1175/BAMS-D-21-0314.1, 2022.

Pommier, M.: Estimations of NOx emissions, NO2 lifetime and their temporal variation over three British urbanised regions in 2019 using TROPOMI NO2 observations, Environmental Science: Atmospheres, https://doi.org/10.1039/D2EA00086E, 2022.

Rastigejev, Y., Park, R., Brenner, M. P., and Jacob, D. J.: Resolving intercontinental pollution plumes in global models of atmospheric transport, Journal of Geophysical Research: Atmospheres, 115, https://doi.org/https://doi.org/10.1029/2009JD012568, 2010.

Rey-Pommier, A., Chevallier, F., Ciais, P., Broquet, G., Christoudias, T., Kushta, J., Hauglustaine, D., and Sciare, J.: Quantifying NOx emissions in Egypt using TROPOMI observations, Atmospheric Chemistry and Physics, 22, 11 505–11 527, https://doi.org/10.5194/ACP-22-11505-2022, 2022.

Riess, C., Boersma, K., Prummel, A., Stratum, B., Laat, J., and Vliet, J.: Estimating NOx Emission of Individual Ships from Tropomi NO2 Plumes, https://doi.org/10.2139/ssrn.4858709, 2024.

Romer Present, P. S., Zare, A., and Cohen, R. C.: The changing role of organic nitrates in the removal and transport of NO_x, Atmospheric Chemistry and Physics, 20, 267–279, https://doi.org/10.5194/acp-20-267-2020, 2020.

Saw, G. K., Dey, S., Kaushal, H., and Lal, K.: Tracking NO2 emission from thermal power plants in North India using TROPOMI data, Atmospheric Environment, 259, https://doi.org/10.1016/J.ATMOSENV.2021.118514, 2021.

Schaap, M., Timmermans, R., Roemer, M., Boersen, G., Builtjes, P., Sauter, F., Velders, G. J. M., and Beck, J.: The LOTOS? EUROS model: description, validation and latest developments, Int. J. Environment and Pollution, 32, https://doi.org/10.1504/IJEP.2008.017106, 2008.

Seinfeld, J. H. and Pandis, S. N.: Atmospheric Chemistry and Physics: From Air Pollution to Climate Change, John Wiley & Sons, Hoboken, New Jersey:, 2nd edn., 2006.

Skoulidou, I., Koukouli, M. E., Segers, A., Manders, A., Balis, D., Stavrakou, T., van Geffen, J., and Eskes, H.: Changes in power plant nox emissions over northwest greece using a data assimilation technique, Atmosphere, 12, https://doi.org/10.3390/ATMOS12070900, 2021a.

Skoulidou, I., Koukouli, M.-E., Manders, A., Segers, A., Karagkiozidis, D., Gratsea, M., Balis, D., Bais, A., Gerasopoulos, E., Stavrakou, T., van Geffen, J., Eskes, H., and Richter, A.: Evaluation of the LOTOS-EUROS NO_2 simulations using ground-based measurements and S5P/TROPOMI observations over Greece, Atmospheric Chemistry and Physics, 21, 5269–5288, https://doi.org/10.5194/acp-21-5269-2021, 2021b.

Sobanski, N., Thieser, J., Schuladen, J., Sauvage, C., Song, W., Williams, J., Lelieveld, J., and Crowley, J. N.: Day and night-time formation of organic nitrates at a forested mountain site in south-west Germany, Atmospheric Chemistry and Physics, 17, 4115–4130, https://doi.org/10.5194/acp-17-4115-2017, 2017.

Song, W., Liu, X. Y., Hu, C. C., Chen, G. Y., Liu, X. J., Walters, W. W., Michalski, G., and Liu, C. Q.: Important contributions of non-fossil fuel nitrogen oxides emissions, Nature Communications 2021 12:1, 12, 1–7, https://doi.org/10.1038/s41467-020-20356-0, 2021.

Timmermans, R., Kranenburg, R., Manders, A., Hendriks, C., Segers, A., Dammers, E., Zhang, Q., Wang, L., Liu, Z., Zeng, L., Denier van der Gon, H., and Schaap, M.: Source apportionment of PM2.5 across China using LOTOS-EUROS, Atmospheric Environment, 164, 370–386, https://doi.org/https://doi.org/10.1016/j.atmosenv.2017.06.003, 2017.

Valin, L. C., Russell, A. R., and Cohen, R. C.: Variations of OH radical in an urban plume inferred from NO2 column measurements, Geophysical Research Letters, 40, 1856–1860, https://doi.org/https://doi.org/10.1002/grl.50267, 2013.

van Geffen, J., Eskes, H., Boersma, K. F., and Veefkind, P.: TROPOMI ATBD of the total and tropospheric NO2 data products. S5P-KNMI-L2-0005-RP, 2022a.

van Geffen, J., Eskes, H., Compernolle, S., Pinardi, G., Verhoelst, T., Lambert, J.-C., Sneep, M., ter Linden, M., Ludewig, A., Boersma, K. F., and Veefkind, J. P.: Sentinel-5P TROPOMI NO_2 retrieval: impact of version v2.2 improvements and comparisons with OMI and ground-based data, Atmospheric Measurement Techniques, 15, 2037–2060, https://doi.org/10.5194/amt-15-2037-2022, 2022b.

Veefkind, P., Aben, I., McMullan, K., Förster, H., Vries, J., Otter, G., Claas, J., Eskes, H., Dehaan, J., Kleipool, Q., van Weele, M., Hasekamp, O., Hoogeveen, R., Landgraf, J., Snel, R., Tol, P., Ingmann, P., Voors, R., Kruizinga, B., and Levelt, P.: TROPOMI on the ESA Sentinel-5 Precursor: A GMES mission for global observations of the atmospheric composition for climate, air quality and ozone layer applications, Remote Sensing of Environment, 120, 70–83, https://doi.org/10.1016/j.rse.2011.09.027, 2012.

Verhoelst, T., Compernolle, S., Pinardi, G., Lambert, J.-C., Eskes, H. J., Eichmann, K.-U., Fjæraa, A. M., Granville, J., Niemeijer, S., Cede, A., Tiefengraber, M., Hendrick, F., Pazmiño, A., Bais, A., Bazureau, A., Boersma, K. F., Bognar, K., Dehn, A., Donner, S., Elokhov, A., Gebetsberger, M., Goutail, F., Grutter de la Mora, M., Gruzdev, A., Gratsea, M., Hansen, G. H., Irie, H., Jepsen, N., Kanaya, Y., Karagkiozidis, D., Kivi, R., Kreher, K., Levelt, P. F., Liu, C., Müller, M., Navarro Comas, M., Piters, A. J. M., Pommereau, J.-P., Portafaix, T., Prados-Roman, C., Puentedura, O., Querel, R., Remmers, J., Richter, A., Rimmer, J., Rivera Cárdenas, C., Saavedra de Miguel, L., Sinyakov, V. P., Stremme, W., Strong, K., Van Roozendael, M., Veefkind, J. P., Wagner, T., Wittrock, F., Yela González, M., and Zehner, C.: Ground-based validation of the Copernicus Sentinel-5P TROPOMI NO_2 measurements with the NDACC ZSL-DOAS, MAX-DOAS and Pandonia global networks, Atmospheric Measurement Techniques, 14, 481–510, https://doi.org/10.5194/amt-14-481-2021, 2021.

Vinken, G. C. M., Boersma, K. F., Jacob, D. J., and Meijer, E. W.: Accounting for non-linear chemistry of ship plumes in the GEOS-Chem global chemistry transport model, Atmospheric Chemistry and Physics, 11, 11 707–11 722, https://doi.org/10.5194/acp-11-11707-2011, 2011.

Vivanco, M. G., Theobald, M. R., García-Gómez, H., Garrido, J. L., Prank, M., Aas, W., Adani, M., Alyuz, U., Andersson, C., Bellasio, R., Bessagnet, B., Bianconi, R., Bieser, J., Brandt, J., Briganti, G., Cappelletti, A., Curci, G., Christensen, J. H., Colette, A., Couvidat, F., Cuvelier, C., D'Isidoro, M., Flemming, J., Fraser, A., Geels, C., Hansen, K. M., Hogrefe, C., Im, U., Jorba, O., Kitwiroon, N., Manders, A., Mircea, M., Otero, N., Pay, M.-T., Pozzoli, L., Solazzo, E., Tsyro, S., Unal, A., Wind, P., and Galmarini, S.: Modeled deposition of nitrogen and sulfur in Europe estimated by 14 air quality model systems: evaluation, effects of changes in emissions and implications for habitat protection, Atmospheric Chemistry and Physics, 18, 10 199–10 218, https://doi.org/10.5194/acp-18-10199-2018, 2018.

Vlemmix, T., Eskes, H. J., Piters, A. J. M., Schaap, M., Sauter, F. J., Kelder, H., and Levelt, P. F.: MAX-DOAS tropospheric nitrogen dioxide column measurements compared with the Lotos-Euros air quality model, Atmospheric Chemistry and Physics, 15, 1313–1330, https://doi.org/10.5194/acp-15-1313-2015, 2015.

Wang, Y., Wang, J., Zhou, M., Henze, D. K., Ge, C., and Wang, W.: Inverse modeling of SO2 and NOx emissions over China using multisensor satellite data - Part 2: Downscaling techniques for air quality analysis and forecasts, Atmospheric Chemistry and Physics, 20, 6651–6670, https://doi.org/10.5194/ACP-20-6651-2020, 2020.

Williams, J. E., Boersma, K. F., Le Sager, P., and Verstraeten, W. W.: The high-resolution version of TM5-MP for optimized satellite retrievals: description and validation, Geoscientific Model Development, 10, 721–750, https://doi.org/10.5194/gmd-10-721-2017, 2017.

Xian, T. and Homeyer, C. R.: Global tropopause altitudes in radiosondes and reanalyses, Atmospheric Chemistry and Physics, 19, 5661–5678, https://doi.org/10.5194/acp-19-5661-2019, 2019.

Xue, R., Wang, S., Zhang, S., He, S., Liu, J., Tanvir, A., and Zhou, B.: Estimating city NOX emissions from TROPOMI high spatial resolution observations – A case study on Yangtze River Delta, China, Urban Climate, 43, https://doi.org/10.1016/J.UCLIM.2022.101150, 2022.

Yarce Botero, A., Lopez-Restrepo, S., Pinel Peláez, N., Quintero, O. L., Segers, A., and Heemink, A. W.: Estimating NOx LOTOS-EUROS CTM Emission Parameters over the Northwest of South America through 4DEnVar TROPOMI NO2 Assimilation, Atmosphere, 12, https://doi.org/10.3390/atmos12121633, 2021.

Zara, M., Boersma, K. F., Eskes, H., Denier van der Gon, H., Vila-Guerau de Arellano, J., Krol, M., van der Swaluw, E., Schuch, W., and Velders, G. J.: Reductions in nitrogen oxides over the Netherlands between 2005 and 2018 observed from space and on the ground: Decreasing emissions and increasing O3 indicate changing NOx chemistry, Atmospheric Environment: X, 9, 100 104, https://doi.org/https://doi.org/10.1016/j.aeaoa.2021.100104, 2021.

Zhang, Q., Boersma, K. F., Zhao, B., Eskes, H., Chen, C., Zheng, H., and Zhang, X.: Quantifying daily NOx and CO2 emissions from Wuhan using satellite observations from TROPOMI and OCO-2, Atmospheric Chemistry and Physics, 23, 551–563, https://doi.org/10.5194/ACP-23-551-2023, 2023.

Zhang, X., van der A, R., Ding, J., Eskes, H., van Geffen, J., Yin, Y., Anema, J., Vagasky, C., Lapierre, J. L., and Kuang, X.: Spaceborne Observations of Lightning NO2 in the Arctic, Environmental Science and Technology, https://doi.org/10.1021/ACS.EST.2C07988, 2022.

Zhao, X., Griffin, D., Fioletov, V., Mclinden, C., Cede, A., Tiefengraber, M., Mueller, M., Bognar, K., Strong, K., Boersma, K., Eskes, H., Davies, J., Ogyu, A., and Lee, S. C.: Assessment of the quality of TROPOMI high-spatial-resolution NO₂ data products in the Greater Toronto Area, Atmospheric Measurement Techniques, 13, 2131–2159, https://doi.org/10.5194/amt-13-2131-2020, 2020.

Zhuang, J., Dussin, R., Huard, D., Bourgault, P., Banihirwe, A., Raynaud, S., Malevich, B., Schupfner, M., Filipe, Levang, S., Gauthier, C., Jüling, A., Almansi, M., RichardScottOZ, RondeauG, Rasp, S., Smith, T. J., Stachelek, J., Plough, M., Pierre, Bell, R., Caneill, R., and Li, X.: pangeo-data/xESMF: v0.8.2 (v0.8.2), Zenodo, https://doi.org/10.5281/zenodo.8356796, 2023.